1
Solubility, Miscibility, and the Impact on Solid-State Morphology

Florian Machui and Christoph J. Brabec

1.1
Introduction

In recent years, organic semiconductors have been of increasing interest in academic and industrial fields. Compared to their inorganic counterparts, they offer various advantages such as ease of processing, mechanical flexibility, and potential in low-cost fabrication of large areas [1]. Furthermore, modifications of the chemical structure allow tailoring material properties and thus enhancing the applicability [2]. After the discovery of metallic conduction in polyacetylene in 1977 by Heeger, MacDiarmid, and Shirakawa, the path was paved for new material classes of electrical conductive polymers, possible due to chemical doping of conjugated polymers. This resulted in an increase of electrical conductivity by several orders of magnitude [3]. The main advantage of organic semiconductors is their processability from solution, which opens different applications such as flat panel displays and illumination, integrated circuits, and energy conversion [4–7]. Before widespread commercial application, further scientific investigations are necessary to achieve improved device performance and environmental stability.

The first organic solar cells were based on an active composite consisting of one single material between two electrodes with different work functions. Light absorption forms Coulomb-bound electron–hole pairs, so-called excitons, which have to be separated for charge generation [8]. In single-material active layers, this is possible by overcoming the exciton binding energy, either thermally or at the contacts [9]. Since both processes have rather low (<1%) efficiencies for pristine organic semiconductors, only few excitons are dissociated and recombination is very dominant. Therefore, single-layer organic solar cells exhibit device efficiencies far below 1% [10]. The first organic bilayer solar cell was presented by Tang, where copper phthalocyanine in combination with a perylene derivative is used as light absorption composite. In bilayer devices, excitons could diffuse within the donor phase toward an interface with a strongly electronegative acceptor material, which provides enough energy for exciton separation [11]. The electron gets transferred to the acceptor (i.e., lower in energy) and the hole remains on the donor. Currently, the most commonly used concept for the active layer in organic photovoltaic

Semiconducting Polymer Composites: Principles, Morphologies, Properties and Applications, First Edition.
Edited by Xiaoniu Yang.

devices is the bulk heterojunction (BHJ), which consists of an interpenetrating network of a hole conductor and an electron acceptor, taking care of the low exciton diffusion length [12]. The main advantage of the BHJ concept is the increased interfacial surface leading to very efficient exciton dissociation within the whole active layer of the solar cell. The most commonly employed materials are conjugated polymers as donors and fullerene derivatives as acceptors [13–16]. By spontaneous phase separation, a specific nanostructure is formed that is decisive for the charge transport, since charge separation takes place at the interface. In the field of organic photovoltaics, several groups have realized devices with efficiencies over 6% [17–20]. Significant improvements have raised certified efficiencies up to 8.3% and novel concepts are under investigation to reach efficiencies beyond 10% (Konarka, http://www.konarka.com; Heliatek, http://www.heliatek.com.) [21].

For an efficient bulk heterojunction solar cell, good control of morphology is a key aspect, which is mainly influenced by the components' solubility during processing, the components' miscibility, and the formation of the resulting film. Solubility describes to what extent a substance dissolves in a particular solvent. This is the key phenomenon with regard to the design of inks and solvent systems with mutual multicomponent solubility regimes. The miscibility of several components in the film is mainly influenced by thermodynamic parameters. Film formation is additionally influenced by the surface energy differences of the substrate to the printing medium as well as by kinetic aspects.

Upscaling from lab to mass production facilities is one of the major necessities for cost optimization. In the case of organic solar cells, this is possible by large-area roll-to-roll processing, allowing throughputs of 10 000 $m^2 h^{-1}$. This is orders of magnitude higher compared to silicon processing capabilities [22]. Currently, the most employed deposition method for organic solar cells is spin coating, since inherent advantages such as high film uniformity and ease of production are suitable for research activities. However, spin coating is very unfavorable for production due to its limitation in size. Doctor blading as an alternative coating technique is more suitable for larger area substrates and is easily transferred to roll-to-roll processing. For all of these techniques, it is necessary to know of the ink's solubility to adjust the formulation. Accordingly, the material parameters for ink definition are viscosity, evaporation rate of the solvent systems, and the spreading behavior. These phenomena together define the quality and the functionality of an organic semiconductor layer. Due to the high technical relevance for organic photovoltaics and, more generally, for organic electronics, the impacts of these phenomena on the performance and functionality of bulk heterojunction composite formation are the major topics in this chapter.

1.2 General Aspects

In general, chlorinated solvents are commonly used for processing in laboratories, which have restricted application in industrial operation due to safety risks and

processing costs. Environment-friendly inks are therefore one decisive criterion for mass production that should provide full functionality. Since solubility is one of the determining factors for processing of the active layer in organic solar cells, several approaches are under investigation to predict solubility of the materials in question.

1.2.1 Solubility

Different approaches can be utilized to determine the solubility of a material. While simulation of solubility is a helpful tool to predict material behavior, experimental verification is of utmost importance. In order to reduce the expensive and time-consuming experimental efforts as well as frequent toxicity issues, simulations are a welcome tool to accompany experiments. One possibility to predict the material solubility is the use of solubility parameters, which was first proposed by Hildebrand and Scott and diversified by Hansen [23, 24]. In this approach, the energy of mixing is related to the vaporization energies of pure components. For liquids as well as for polymers, the solubility parameter δ was defined as the square root of the cohesive energy density (CED) with ΔE_v as energy of vaporization and V_m as average molar volume. Here the energy of mixing is related to the energies of vaporization of the pure components according to Eqs. (1.1)–(1.3). The contributions to ΔE_v in Eq. (1.2) are the difference in enthalpy of evaporation ΔH, the absolute temperature T, and the global ideal gas constant R.

$$\delta = \mathrm{CED}^{1/2} = (\Delta E_v / V_m)^{1/2}, \tag{1.1}$$

$$\Delta E_v = \Delta H - RT. \tag{1.2}$$

Blanks, Prausnitz, and Weimer assigned the separation of vaporization energy into a nonpolar, dispersive part and a polar part [25, 26]. The polar part was further divided into dipole–dipole contribution and hydrogen bonding contribution by Hansen with δ_D as solubility parameter due to dispersion forces, δ_P as solubility parameter due to polar dipole forces, and δ_H as solubility parameter due to hydrogen bonding interactions according to Eq. (1.3) [27–29].

$$\delta^2 = \delta_D^2 + \delta_P^2 + \delta_H^2. \tag{1.3}$$

Hansen solubility properties are usually plotted in a three-dimensional coordinate system with the Hansen parameters as x, y, z axes. The coordinates of a solute can be determined by analyzing the solubility of a solute in a series of solvents with known Hansen parameters. By fitting a spheroid into the solubility space, the solubility volume of this solute can be identified. The solubility space of a solute is defined by the origin of a spheroid, resulting from the three coordinates, and the three radii in each dimension, with solvents inside the spheroid and nonsolvents outside. The radius of the sphere, R_0, indicates the maximum difference for solubility. Generally, good solvents are within the sphere, and bad ones are outside of it. Furthermore, the solubility "distance"

parameter, R_a, between one solvent and one solute reflecting their respective partial solubility parameters can be defined with Eq. (1.4), with δ_{D2} as dispersive component for the solvent, δ_{D1} as dispersive component of the solute, and a, b, and c as weighting factors. Setting of $a = 4$ and $b = c = 1$ was suggested by Hansen based on empirical testing. To convert the Hansen spheroid into an ellipsoid, different ratios of weighting factors are used. When the scale for the dispersion parameter is doubled, the spheroidal shaped volume is converted into a spherical body [24].

$$R_a^2 = a(\delta_{D2} - \delta_{D1})^2 + b(\delta_{P2} - \delta_{P1})^2 + c(\delta_{H2} - \delta_{H1})^2. \tag{1.4}$$

Further studies by Small revealed that solubility parameters of polymers could also be calculated by using group contribution methods, which was intensified by Hoy, van Krevelen, and Coleman *et al.* [30–33]. The properties of molecules are investigated by separating them into smaller subgroups. The basic assumption is that the free energy of a molecule transfer between two phases is the sum of its individual contributions of groups, and that these group contributions are independent of the rest of the molecule. There is an obvious trade-off in group contributions. It is possible to define several groups in different ways. The more the subgroups used, the more accurate the group contributions become, but the less likely that there is sufficient statistical data to make predictions. More examples have been employed elsewhere [34–36]. For predicting solubility parameters using the group contribution method, frequently the following approach is used with F_i as molar attraction constant of a specific group i and V_m as molar volume:

$$\delta = \left| \frac{\sum F_i}{V_m} \right|. \tag{1.5}$$

Another method to predict solubility of solutes in different solvents is based on the prediction of the activity coefficient using density functional theory [37]. Molecules exhibit a rigid structure, but can possess different conformations, whose physical and chemical properties depend on their ultimate three-dimensional confirmation. Jork *et al.* showed that different conformations have different influence on the predictions of the activity coefficient [38]. Klamt *et al.* introduced a conductor-like screening model for real solvents (COSMO-RS), which allows a priori calculation of chemical potentials of one component within an arbitrary environment [39–42]. Here, modeling is realized by statistical thermodynamics where interacting molecules are substituted by corresponding pairwise interacting surface segments with densely packed contact areas. Since every segment has a constant charge density σ, the characterization of a molecule is possible by knowing the distribution function of the charge density $P(\sigma)$, the σ-profile. With that the properties of the molecules are solely dependent on the number of segments. The σ-profile of a pure component results directly from the density functional theory calculation. Further methods are based on molecular dynamics or Monte Carlo simulations but discussions are beyond the topic of this chapter.

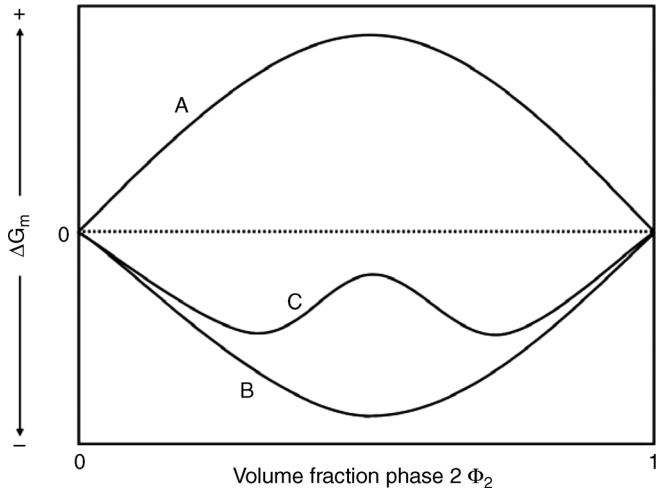

Figure 1.1 Gibbs free energy of mixing as a function of composition. (According to Refs. [43, 44].)

1.2.2
Miscibility–Thermodynamic Relationships

A decisive criterion of organic semiconductor applications is their ability of mixing. In general, blends of two or more components can be categorized according to the miscibility of their phases in one-phase or multiphase systems. Miscibility is usually defined by thermodynamic parameters. Here the Gibbs free mixing enthalpy ΔG_m is decisive for compatibility of two phases. Figure 1.1 shows the Gibbs free energy as a function of compositions. If ΔG_m is positive, the components are not miscible (A). If ΔG_m is negative and the second derivative is positive, both components are totally miscible (B). Independent of composition, a homogeneous blend is formed. If ΔG_m is negative and the second derivative is negative as well, the components are partially miscible (C). Phases with different composition are formed, which consist of both components [43, 44].

$$\Delta G_m = \Delta H_m - T\Delta S_m. \tag{1.6}$$

ΔG_m can be determined according by changes in enthalpy (ΔH_m) and entropy of mixing the components (ΔS_m). Compared to low molecular mass components, the entropy increase is low for mixing polymers. Mixing of two polymers results in a smaller increase of ΔS_m as compared to a binary blend of two low molecular weight components. Therefore, according to Eq. (1.6), the enthalpy change is the decisive parameter for thermodynamic miscibility [43]. The relatively smaller increase of entropy for polymers versus small molecules can be explained with Figure 1.2. The two-dimensional grids in Figure 1.2 represent places for molecules or for polymer segments. The number of possible configurations W is significantly higher for the

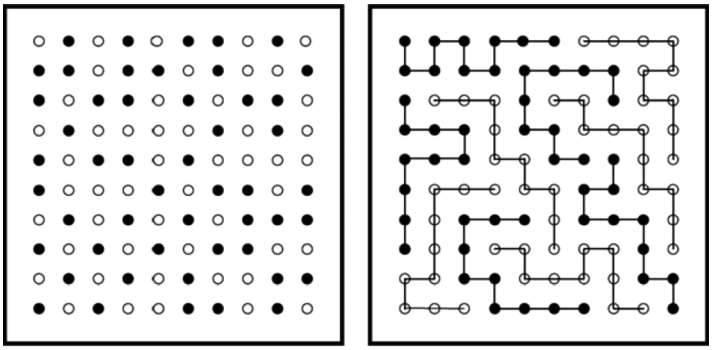

Figure 1.2 Schematic depiction of blends with components of smaller molar mass (a) and higher molar mass (a). (According to Refs [43, 44].)

arrangement with the small molecules. With $S \sim kT\ln(W)$, the lower entropy increase for polymer blends becomes obvious.

Since Gibbs free energy ΔG_m cannot be determined directly, thermodynamic models are used for the estimation. An often used model for polymer–polymer systems is the Flory–Huggins theory [45]. The Flory–Huggins definition of the Gibbs free energy and its implication on polymer blends are discussed in Eq. (1.7). It describes the free energy of binary systems, with the first two parts of the equation representing the entropic part and the third part describing the enthalpic phenomena. Here, φ_i is the volume fraction of component i, V_i is the molar volume of component i, B_{12} is the interaction parameter, and R is the ideal gas constant. In the case of polymer blends, the free energy is dominated by the enthalpic changes, which need to be negative for miscible systems. ΔH_m is directly proportional to the number of interactions between the two components, and becomes negative for strong interactions such as ion, acid–base, hydrogen bonds, or dipole–dipole interactions.

$$\Delta G_m = \left(\frac{\varphi_1}{V_1}\ln\varphi_1 + \frac{\varphi_2}{V_2}\ln\varphi_2 + \varphi_1\varphi_2 B_{12}\right) RTV. \tag{1.7}$$

1.3 Solubility, Solvents, and Solution Formulations

1.3.1 Solubility

In this chapter, the solubility of organic semiconductors, their influence on OPV devices, and their correlation with Hansen solubility parameters (HSPs) are discussed. Before that, experimental methods to determine the absolute solubility of organic semiconductors are reviewed. High-performance liquid chromatography

(HPLC) is a separation method to identify and quantify exact concentrations of nonvolatile components. Saturated filtered solutions are analyzed and compared with standard solutions with known concentrations [48]. Spectrophotometrical measurements are also a commonly used method to determine the absolute solubility. First, saturated solutions are filtered or centrifuged to obtain true solutions. Next, these solutions are further diluted and characterized by optical absorption measurements. By comparing the optical density (OD) of the investigated solutions with the OD of calibrated master solutions, the solubility of the component in the investigated media can be determined. Examples for determination of organic semiconductor solubility measurements with this method have been reported by Walker *et al.* and Machui *et al.* [46, 47].

Ruoff *et al.* analyzed the solubility of pure C_{60} in different solvents [48]. HPLC was used to measure the solubility at room temperature in 47 solvents. Categorizing the solvents according to their chemical structure helped to identify good solvents such as naphthalenes and halogenated aromatics. In the first study on conjugated polymer:fullerene bulk heterojunction solar cells, the limited solubility of pure C_{60} in organic solvents and their tendency to crystallize during film formation was recognized by members of the Heeger group [12, 49]. Homogeneous stable blends with more than 80 wt% fullerene content became processable by the use of soluble C_{60} derivatives such as [6,6]-phenyl-C_{61}-butyric acid methyl ester ($PC_{61}BM$). A rough estimation of the solubility of $PC_{61}BM$ in toluene and chlorobenzene (CB) was achieved via saturated solutions by Hoppe and Sariciftci and reported with 1 wt% in toluene and 4.2 wt% in CB [64]. Kronholm and Hummelen later on published solubility values for $PC_{61}BM$ and [6,6]-phenyl-C_{71}-butyric acid methyl ester ($PC_{71}BM$) in different aromatic solvents, that is, toluene, *p*-xylene, *o*-xylene, CB, chloroform, and 1,2-dichlorobenzene (*o*-DCB) [50]. Solubility was determined by HPLC analysis of the liquid phase at room temperature. For both $PC_{61}BM$ and $PC_{71}BM$, highest solubility was found in *o*-DCB (30 mg ml^{-1} for $PC_{61}BM$), followed by CB and chloroform (each 25 mg ml^{-1}) and *o*-xylene, toluene, and *p*-xylene ($<$20 mg ml^{-1}). $PC_{71}BM$ was in all cases better soluble than $PC_{61}BM$. Troshin *et al.* analyzed the solubility of different fullerene derivatives and compared them to the resulting device performance, which is shown in Figure 1.3 [51]. Especially remarkable is a steep increase of short-circuit current density (J_{SC}), fill factor (FF), and power conversion efficiency (PCE, η) for increasing fullerene solubility in CB from 0 to about 40 mg ml^{-1}. Higher solubility values of about 60 mg ml^{-1} again resulted in a decrease of device performance. For open-circuit voltage (V_{OC}), an increase until a solubility of 30 mg ml^{-1} was recognizable. Higher solubility values did not change V_{OC}.

Hansen and Smith introduced Hansen solubility parameters for organic semiconductors and analyzed pristine C_{60} in organic solvents [52]. It was concluded that C_{60} would be soluble in polymers with aromatic rings or atoms that are significantly larger than carbon, such as sulfur or chlorine. The temperature-dependent solubility and the mutual solubility regimes for poly(3-hexylthiophene-2,5-diyl) (P3HT), $PC_{61}BM$, and small bandgap polymer-bridged bithiophene poly[2,6-(4,4-bis-(2-ethylhexyl)-4*H*-cyclopenta[2,1-*b*;3,4-*b*′]-dithiophene)-*alt*-4,7-(2,1,3-

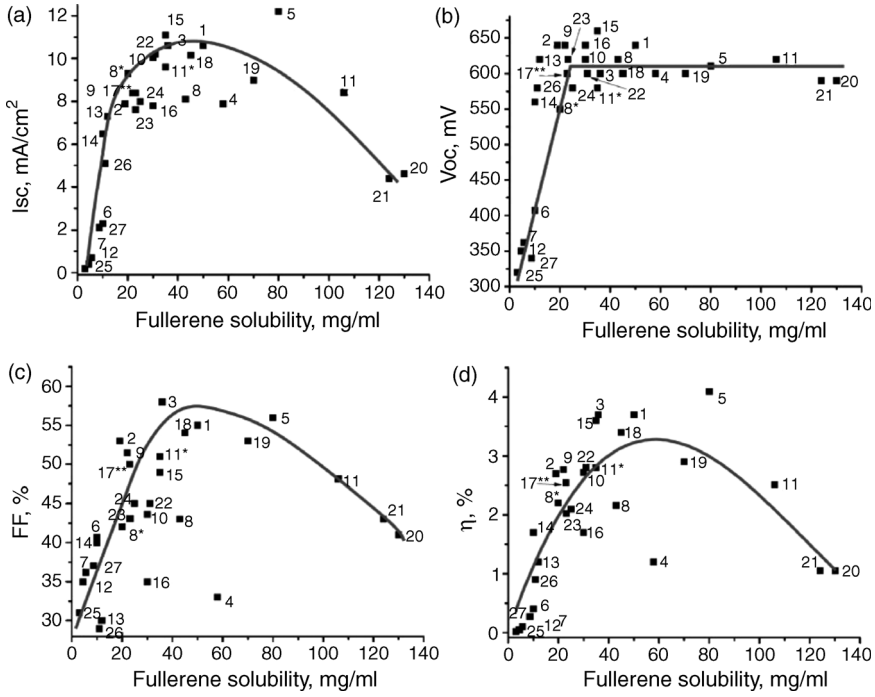

Figure 1.3 (a–d) Relationship between solar cell output parameters (I_{SC}, V_{OC}, FF, and η, respectively) and solubility of the fullerene derivative used as electron-acceptor material in the active layer. The lines are included as a guide for the eye. (From Ref. [51].)

benzothiadiazole)] (PCPDTBT) have been analyzed [47]. For the dominantly amorphous polymer PCPDTBT and the fullerene, results showed a good consistency over a broad temperature regime. Due to the semicrystalline character of P3HT, an exact determination of the solubility parameters was found difficult in a temperature regime of 25–140 °C. With increasing temperature, the solubility radius of P3HT increases significantly as well, which was explained by breaking of aggregates at elevated temperatures. Mutual solubility regimes for all three components have been identified as shown in Figure 1.4. For P3HT, the HSP parameters at 60 °C were reported as $\delta_D = 18.7\,MPa^{1/2}$, $\delta_P = 1.4\,MPa^{1/2}$, $\delta_H = 4.5\,MPa^{1/2}$, and solubility radius $R_0 = 4.3\,MPa^{1/2}$. The δ_D, δ_P, δ_H, and R_0 values were determined to be 17.3, 3.6, 8.7, and 8.2 $MPa^{1/2}$ for PCPDTBT and 18.7, 4.0, 6.1, and 7.0 $MPa^{1/2}$ for $PC_{61}BM$, respectively, at 60 °C.

Park *et al*. used Hansen solubility parameters and showed that non-halogenated solvent blends with the same Hansen parameters as *o*-DCB can be used to reach comparable device performance [53]. They mixed mesitylene (MS) with acetophenone (AP) in different ratios to match *o*-DCB Hansen parameters. Different mixtures of AP and MS were used with different ratios resulting in PCEs ranging from 1.5% (pure MS) to 3.38% (20 vol.% acetophenone) for P3HT:$PC_{61}BM$ cells with best external quantum efficiency (EQE) match with *o*-DCB. This has so far been

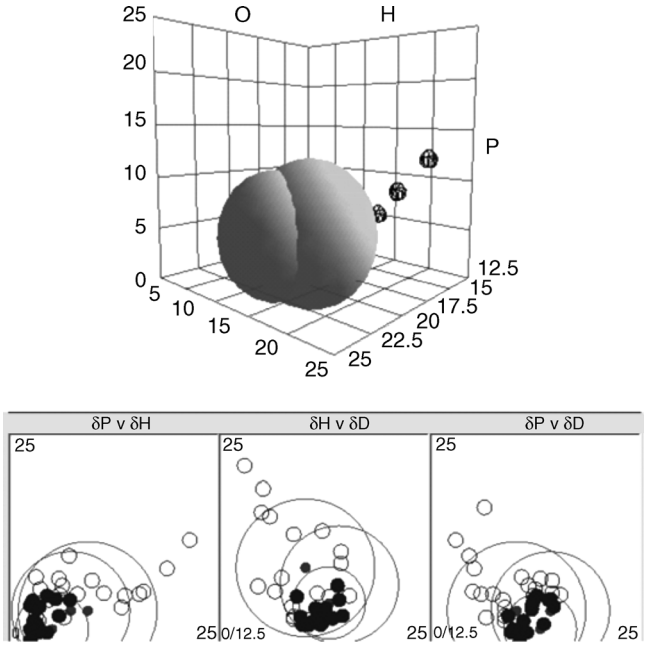

Figure 1.4 HSP diagram for solutes at 60 °C with 34 solvents, 2.5 g l^{-1} for P3HT, PCPDTBT, and $PC_{61}BM$. (From Ref. [47].)

the first combination for solvent blends and Hansen solubility parameters for organic semiconductors. Walker *et al.* analyzed a conjugated polymer 3,6-bis(5-(benzofuran-2-yl)thiophen-2-yl)-2,5-bis(2-ethylhexyl)pyrrolo[3,4-*c*]pyrrole-1,4-dione (DPP(TBFu)$_2$) and $PC_{71}BM$ [46]. The solvents were classified into good, intermediate, and poor solvents. For $PC_{71}BM$, mostly higher solubility values were found in comparison to $PC_{61}BM$. The average δ_D, δ_P, and δ_H parameters were 19.33 ± 0.05, 4.78 ± 0.50, and $6.26 \pm 0.48\,MPa^{1/2}$, respectively, for DPP(TBFu)$_2$ and 20.16 ± 0.28, 5.37 ± 0.80, and $4.49 \pm 0.57\,MPa^{1/2}$, respectively, for $PC_{71}BM$. Atomic force microscopy (AFM) images of films prepared with chloroform, thiophene, trichloroethylene, and carbon disulfide were compared before and after annealing at 110 °C for 10 min. As-cast devices with the different solvents showed poor efficiencies. This is in agreement with the AFM images showing little phase separation. Annealing improves the PCE with efficiencies of up to 4.2% for carbon disulfide and 4.3% for chloroform. It was concluded that good solvents for both components result in optimal phase separation after annealing and HSPs could be used as a general tool for designing and understanding of solution-processed devices.

1.3.2 Solvents

As the active layer of organic solar cells is typically processed from solution, morphology is mainly determined by interactions between the used semiconductor

solutes and the solvent during film formation. In this chapter, the influence of the used solvent on the resulting morphology and thus device performance is discussed. Different approaches to manipulate the morphology by solution processing methods are introduced.

1.3.2.1 Impact of Different Solvents on the Solid-State Morphology

Generally, good device efficiencies require the use of solvents that contain halogens (e.g., chloroform (CF), CB, *o*-DCB, and 1,2,4-trichlorobenzene (TCB)), whose toxicity poses potential problems for manufacturing [54–60]. Dang *et al.* compared different publications of P3HT:$PC_{61}BM$ analyzing material parameters and resulting device efficiencies including a comparison of different solvents and device performance [61]. For the most popular solvents such as CB and *o*-DCB, most PCEs were in the range of 2.5–4%. However, reports for other solvents for device processing such as CF, toluene, xylene, and tetrahydronaphthalene with also high efficiencies were found.

The choice of solvent has a great influence on the resulting morphology and thus on the device performance. This phenomenon was observed in case of poly [2-methoxy-5-(3,7-dimethyloctyloxy)]-1,4-phenylenevinylene (MDMO-PPV) blended with $PC_{61}BM$ by Shaheen *et al.*, who compared toluene and CB as processing solvents [62]. They found a threefold better device performance for CB-processed cells, mainly attributed to higher short-circuit current density and better fill factor due to the better solubility of both components in CB (Figure 1.5). AFM images showed a smaller scale of phase separation, that is, smaller $PC_{61}BM$-rich domains in MDMO-PPV-rich matrix suppressing phase segregation of $PC_{61}BM$ molecules into clusters, and smoother surface roughness that improved the interface contacts to the cathode.

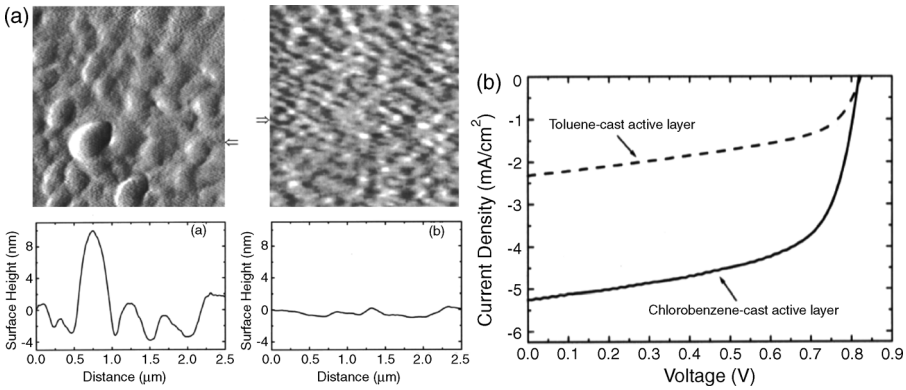

Figure 1.5 (a) AFM images showing the surface morphology of MDMO-PPV:$PC_{61}BM$ blend films when spin coated from a toluene solution (left) and from a CB solution (right). The images show the first derivative of the actual surface heights. The cross sections of the true surface heights for the films were taken horizontally from the points indicated by the arrow. (b) Characteristics for devices with an active layer that is spin coated from a toluene solution (dashed line) and from a CB solution (full line). (From Ref. [62].)

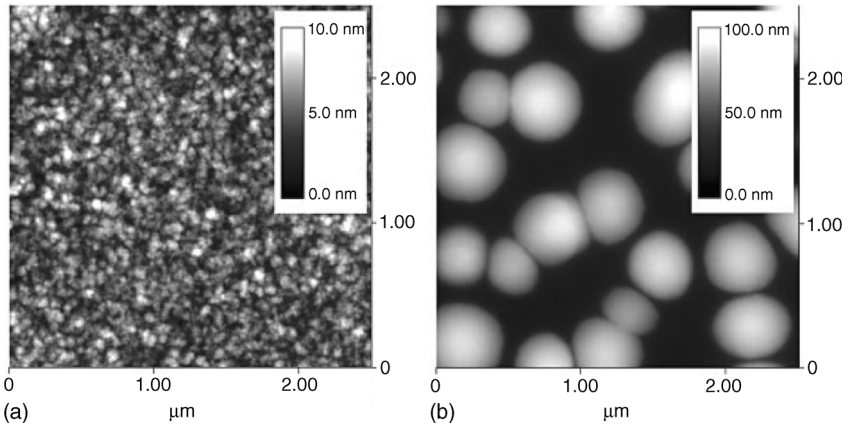

Figure 1.6 Tapping mode AFM topography scans of MDMO-PPV:$PC_{61}BM$ 1 : 4 (by weight) blended films, spin cast from CB (a) and toluene (b) solution. The toluene-cast film exhibits height variations that are one order of magnitude larger than those on CB-cast films. Features of a few hundred nanometers in width are visible in (a), while features in (b) are around 50 nm. (Reproduced from Ref. [63].)

Hoppe *et al*. further investigated the influence of various solvents on the morphology [63, 64]. For toluene as processing solvent, photoluminescence (PL) measurements indicated pure $PC_{61}BM$ clusters with larger extent than exciton diffusion range. PL measurements also showed increased material phase separation after annealing and a photocurrent loss due to $PC_{61}BM$ clusters. Phase separation for toluene was dependent on blend ratio and solute concentration. The comparison of $PC_{61}BM$ in toluene and CB showed larger $PC_{61}BM$ clusters in case of using the poorer solvent toluene as shown in Figure 1.6 [63].

For MDMO-PPV:$PC_{61}BM$, Rispens *et al*. analyzed the influence of solvents on crystal structure of $PC_{61}BM$ as shown in Figure 1.7 [65]. A comparison of *o*-DCB, CB, and xylene as spin casting solvent showed that CB was the best choice as processing solvent. Single $PC_{61}BM$ crystals were obtained from CB resulting in

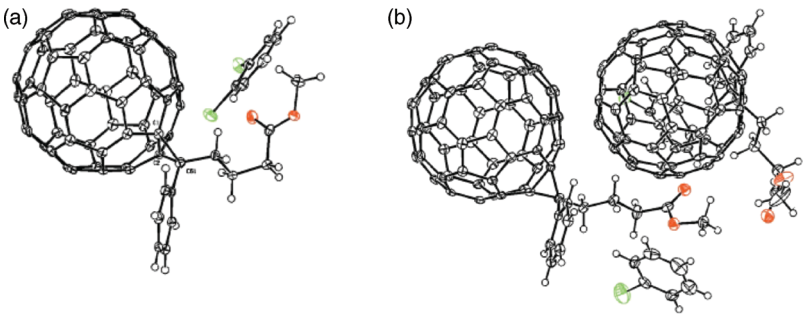

Figure 1.7 Molecular structure of $PC_{61}BM$, crystallized from (a) *o*-DCB and (b) CB (red = oxygen; green = chlorine). (From Ref. [65].)

significantly higher charge mobility than from other solvents resulting in amorphous confirmations.

The influence of different solvents on morphology was also investigated by Ruderer *et al*. for P3HT and $PC_{61}BM$ [66]. Spin-coated films with processing solvents such as CF, toluene, CB, and xylene were investigated by optical microscopy, grazing incidence wide-angle X-ray scattering (GIWAXS), AFM, X-ray reflectivity (XRR), and grazing incidence small-angle X-ray scattering (GISAXS) investigations. Using this wide range of investigation tools led to good understanding of how processing solvents can manipulate the lateral and vertical phase separation. Major influence on device performance resulted from vertical phase separation. $PC_{61}BM$ clusters were formed for low-solubility solvents. P3HT crystallinity was mainly influenced by annealing, and increased with higher boiling point of the solvent attributed to longer drying time during spin coating. The lattice constants were independent for the used solvents. Figure 1.8 shows the schematic vertical morphology resulting from different solvents for P3HT (white areas) and $PC_{61}BM$ (black areas), neglecting phases containing both components. These structures were reconstructed representing the findings with aforementioned methods, suggesting vertical nanostructures for CF-, toluene-, CB-, and xylene-processed films. For toluene-, CB-, and xylene-processed films, lateral nanostructures were found. P3HT accumulation at the bottom was found for toluene- and CB-processed films, while $PC_{61}BM$ accumulation at the bottom was found for chloroform and xylene. P3HT enrichment at the bottom and $PC_{61}BM$ accumulation at the top are considered as advantageous for the "normal" device architecture. Nevertheless, there was no great difference in device performance for all four solvents. It was concluded that lateral and vertical structures are not the only determining factors as long as the phase separation and the material distribution are in the range of the exciton diffusion length (here from 35 to 65 nm) and percolation paths are recognizable.

Yu compared the influence of different solvents on device performance [67]. As processing solvents, CF, CB, *o*-DCB, and TCB were used. According to absorption and PL measurements, charge transport dark current density–voltage (*j*–*V*) curve, XRD pattern, and AFM images, a higher P3HT crystallinity for higher boiling point solvents was concluded, since polymer chains have longer time for self-organization. This resulted in increased absorption and charge carrier mobility leading to

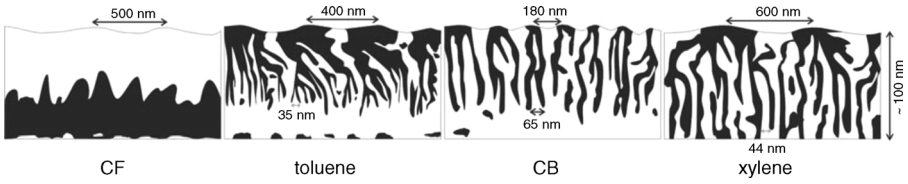

Figure 1.8 Black and white schematic morphology of annealed P3HT:$PC_{61}BM$ films made using CF, toluene, CB, and xylene solutions, as reconstructed from the results of AFM, XRR, and GISAXS investigations. Black areas correspond to pure $PC_{61}BM$ phases and white to pure P3HT phases. Characteristic lengths are indicated. (Reprinted from Ref. [66].)

higher device performance for high boiling point solvent-processed devices. Kwong *et al.* processed P3HT:TiO_2 nanocomposite solar cells using different solvents for spin coating the active layer [68]. A comparison of tetrahydrofuran (THF), CB, CF, and xylene showed that device performance can be strongly influenced by the used solvent. Best cells in this case were achieved with xylene. It was concluded that a good solvent for P3HT with a low evaporation rate may improve the mixing of the components resulting in better exciton dissociation and short-circuit current density. AFM studies showed that the roughest surface was obtained for films spin coated from xylene. Park *et al.* compared the influence of different solvents on solar cells made of the copolymer poly[*N*-9″-heptadecanyl-2,7-carbazole-*alt*-5,5-(4′,7′-di-2-thienyl-2′,1′,3′-benzothiadiazole)] (PCDTBT) in bulk heterojunction composites with the fullerene derivative $PC_{71}BM$ [69]. Transmission electron microscopy (TEM) and AFM comparison for CF-, CB-, and *o*-DCB-processed films showed a decreased phase separation with decreasing volatility of solvents and a higher incident photon to electron conversion efficiency (IPCE).

Jaczewska *et al.* presented a polymer–solvent diagram including film structures for polystyrene (PS):polythiophene blends (1 : 1, w/w) for different processing solvents [70]. Structures were observed with different microscopic techniques, and solubility parameters were used for establishing a polymer–solubility versus solvent–solubility relation. A relation between film morphology and stability of the layers showed a dependence on the surface energy. Dewetting effects could be inhibited by decreasing polythiophene content. Furthermore, a ternary phase diagram was developed for the system polymer, fullerene, and solvent [64]. At constant temperature and pressure, a schematic diagram is shown in Figure 1.9. A decreasing amount of solvent leads to higher repulsive interactions between polymer and

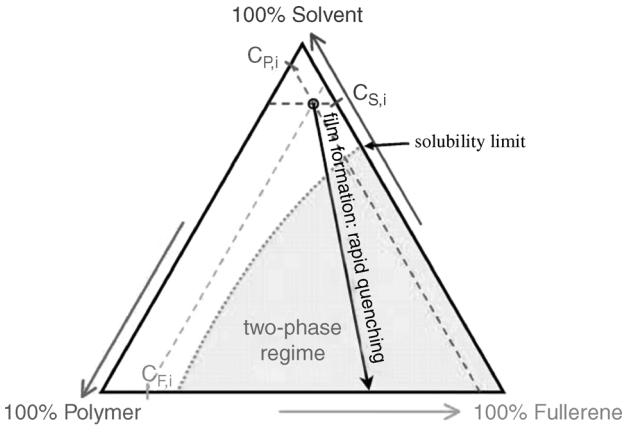

Figure 1.9 Schematic ternary phase diagram of a polymer–fullerene–solvent system at constant temperature T and constant pressure p. The arrows indicate the direction of increasing concentration; $C_{S,i}$, $C_{P,i}$, and $C_{F,i}$ are the initial concentrations of solvent, polymer, and fullerene in the solution, respectively. During film formation, a more or less rapid quenching of the solution toward a solid-state blend takes place upon extraction of the solvent. (Adapted from Ref. [64].)

fullerene molecules. Removing the solvent quickly enough can freeze the blend morphology of the polymer and the fullerene, because phase separation is a temperature-dependent process in time and the system is quenched in a metastable state. Thermal annealing does reactivate the molecule mobility and allows a reorientation and eventual recrystallization of the polymer chains within the composite. In case of very slow drying (i.e., for high boiling point solvents), molecules have more time to orient resulting in higher phase separation and larger domains.

1.3.2.2 **Non-Halogenic Solvents**

Xylene is an often used non-halogenic solvent that frequently offers comparable device performance as with halogenated solvents [61]. *p*-Xylene was used by Berson *et al*. to form P3HT nanofibers [71]. P3HT was previously dissolved in *p*-xylene at elevated temperatures. Nanofibers are formed after cooling to room temperature without precipitations for concentrations in a range of 0.5–3 wt% as shown in Figure 1.10. The time-dependent formation of nanofibers is monitored for a solution of P3HT in *p*-xylene. With more concentrated *p*-xylene solutions, a homogeneous thick film is obtained, which is crucial for the fabrication of photovoltaic active layers. The dimensions of the nanostructures have been determined from the AFM images; the nanofibers had lengths ranging from 0.5 to 5 μm, thicknesses ranging from 5 to 15 nm, and widths ranging from 30 to 50 nm. Moreover, cyclohexanone was also used for fiber formation. A network of fibers was obtained by using a dilute solution in cyclohexanone. Overall, this method resulted in device efficiencies of 3.4% for P3HT:$PC_{61}BM$ blends with no further need of annealing.

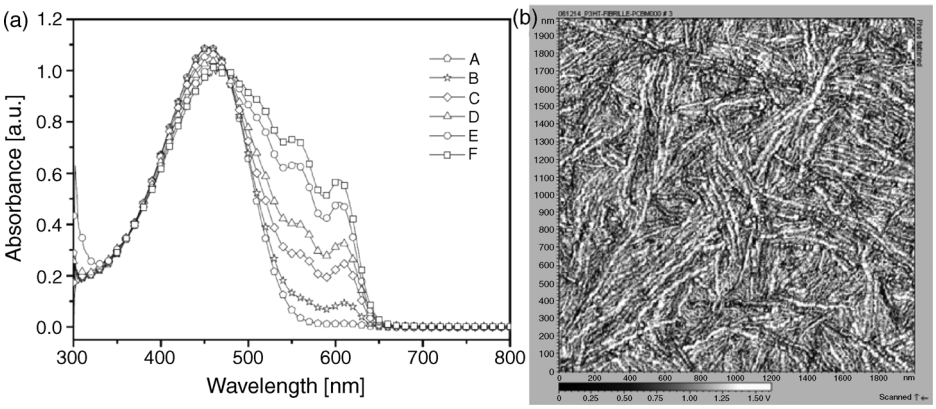

Figure 1.10 (a) Absorption spectra of a 1 wt% solution of P3HT in *p*-xylene heated at 80 °C to ensure complete dissolution of the polymeric material and then allowed to evolve after cooling to room temperature for (A) 2, (B) 4, (C) 6, (D) 21, (E) 28, and (F) 48 h. The solutions are cooled at a rate of 20 °C h^{-1}. (b) AFM phase images of a pristine nanostructured P3HT:$PC_{61}BM$ film deposited on glass from a *p*-xylene solution containing 1 wt% P3HT and 1 wt% $PC_{61}BM$. (From Ref. [71].)

Due to the toxicity and processing problems of halogenic solvents, replacements with non-halogenic solvents gained interest as a concept to lower safety risks and processing costs while keeping the device performance high. Tetralene (1,2,3,4-tetrahydronaphthalene) was first suggested by Hoth *et al.* [72]. Tetralene is a high-boiling solvent showing a lower surface tension compared to *o*-DCB. The tetralene formulation provided reliable inkjet printing, but suffered from poor morphology and significantly rougher surfaces demonstrated in AFM images. This is specific to the inkjet-printed trials since doctor-bladed cells fabricated using tetralene produced cells with PCE of 3.3% for P3HT:$PC_{61}BM$ [73]. Furthermore, toluene was used as a processing solvent. As mentioned previously, device performance is limited due to the lower solubility compared to halogenated solvents resulting in the formation of $PC_{61}BM$ clusters, which restrain the charge separation [62–64].

1.3.2.3 **Solvent Blends**

Solvent blends can be used for device fabrication since they offer the possibility to adjust the morphology via the different solubility of the solutes in the various systems. For devices containing P3HT and $PC_{61}BM$, different groups investigated the influence of solvent mixtures. Kawano *et al.* reported that cells processed with a solvent mixture of *o*-DCB/CF in 60/40 (v/v) ratio had a better performance than the cells prepared from CB [74]. After annealing at 150 °C for 5 min, the cosolvent system achieved an efficiency of 3.73% compared to 3.34% for CB cells. Short-circuit current density and fill factor increased for the cosolvent system due to larger interfacial area between P3HT and $PC_{61}BM$. It was found that the cell efficiency improved by adding moderate amount of CF. The highest cell efficiency was obtained, when 40 vol% CF was added into *o*-DCB. Higher amounts of CF led to a drop in PCE. Furthermore, surface morphology was investigated, which showed that surface roughness was higher for the cosolvent system indicating a higher P3HT chain ordering. Lange *et al.* investigated the influence of adding TCB to CB as processing solvent [75]. Changes in the absorption spectra compared to the pure solvents where the P3HT absorption maximum occurred between the maxima of the two pure solvents. Therefore, it was concluded that adding TCB with a higher boiling point provides P3HT chains more time to form higher crystalline parts. Chen *et al.* mixed *o*-DCB with 1-chloronaphthalene, also providing a higher boiling point compared to *o*-DCB [76]. Absorption spectra showed again a redshift upon addition of the high boiling point solvent 1-chloronaphthalene indicating higher order due to longer time for self-organization. The cell efficiency peaked for 5 vol% 1-chloronaphthalene at 4.3%. *o*-DCB and mesitylene formulations (ratio 68 : 32) were used by Hoth *et al.* for inkjet-printed solar cells achieving PCE of 3% [72]. The solvent blend ratio was chosen to optimize droplet formation properties according to drop volume, velocity, and angularity of the inkjet print head. The combination of *o*-DCB and mesitylene served two purposes: *o*-DCB with the higher boiling point of 180 °C was used to prevent nozzle clogging and provided a reliable jetting of the print head, and mesitylene had a lower surface tension and was used to achieve optimum wetting and spreading of the solution on the substrate. Furthermore, it offered a higher vapor pressure and a lower boiling point compared to *o*-DCB and

increased the drying rate of the solvent mixture, which is a critical parameter for phase separation. High-boiling solvents such as *o*-DCB or tetralene are an essential concept to develop inks for inkjet printing.

Influence of solvent blends was also investigated for blends of a polyfluorene copolymer poly(2,7-(9,9-dioctylfluorene)-*alt*-5,5-(4′,7′-di-2-thienyl-2′,1′,3′-benzothiadiazole)) (APFO-3) with $PC_{61}BM$ for CF, as well as solvent mixtures containing 1.2% CB, xylene, and toluene offering lower vapor pressure as compared to CF [77]. An increase in photocurrent for CF/CB blends was correlated with a finer phase separation, and a decrease in photocurrent for CF/toluene and CF/xylene was attributed to rougher surface morphologies. Furthermore, time-resolved spectroscopy supported morphological results. Wang *et al*. used blends of *o*-DCB and toluene for poly[2,3-bis-(3-octyloxyphenyl)quinoxaline-5,8-diyl-*alt*-thiophene-2,5-diyl] (TQ1) mixed with $PC_{71}BM$ resulting in PCEs of 4.5% [78]. Results suggest that only 5–20 vol.% *o*-DCB in the solvent blend system significantly increased J_{SC}, FF, and PCE. The differences to pure *o*-DCB were quite small. AFM topography images of the spin-coated films showed big grains in the range of 1 μm for films from pure toluene. Grain size decreased to 100 nm by adding 5 vol.% *o*-DCB, which corresponded well to the improved device performance. Smallest grain size resulted from pure *o*-DCB with the best efficiencies. The effect of mixed solvent was also studied for PCDTBT and $PC_{71}BM$ by Alem *et al*. [79]. CF and *o*-DCB were used as good solvents for these two materials. CF-processed films exhibited larger domains, showing increasing size with higher $PC_{71}BM$ content. The 1 : 1 mixing of CF and *o*-DCB was used for realizing optimum domain size resulting in power conversion efficiencies of up to 6.1%. Solvent blends containing CB and *o*-DCB were used for devices made from PCDTBT:$PC_{71}BM$ [69]. Increasing the amount of *o*-DCB in the CB/*o*-DCB mixture increased the contribution from $PC_{71}BM$ to the IPCE, showing pronounced peaks around 400 and 450 nm. *o*-DCB films showed significantly smaller phase separation. Overall, the increased IPCE could be correlated with the nanoscale phase separation.

1.3.2.4 **Addition of Poor Solvents**

Addition of nonsolvents to solvents can result in aggregate formation, which enhances the field-effect mobility of conjugated semiconductors. Park *et al*. added acetonitrile to chloroform and changed the P3HT organization from random coil conformation to an ordered aggregate structure [80]. Besides acetonitrile, different solvents such as hexane, acetone, ethanol, and dimethylformamide were added to chloroform-based P3HT inks as conformation modifiers. P3HT aggregation occurred at a certain solvent ratio and an additional redshifted absorption band appeared. Pristine P3HT–chloroform solution contained one peak at 455 nm, which was associated with intrachain π–π^* transition. For good solvents such as chloroform, P3HT chains were well dissolved, so no sign of molecular ordering occurred. Redshift of the absorption maximum and additional absorption bands was usually associated with ordered aggregates and interchain π–π stacking of P3HT. Both were related to an increased effective conjugation length of the chain segments in the P3HT solution, thereby decreasing energies. Moulé and Meerholz used nitrobenzene (NtB) as nonsolvent for P3HT:$PC_{61}BM$ in CB-based inks [81].

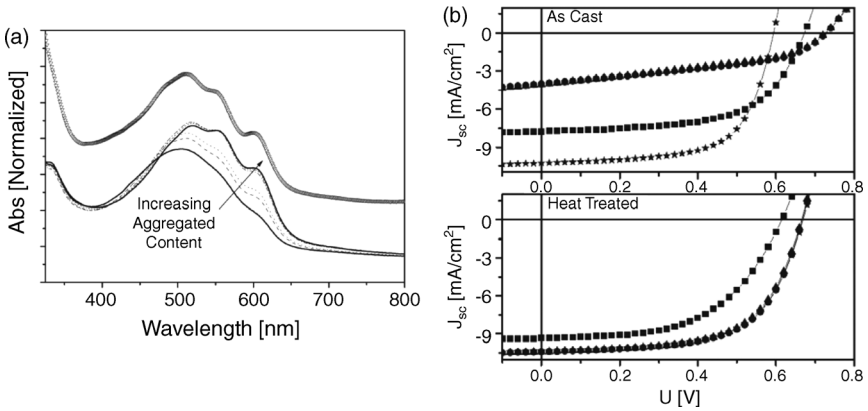

Figure 1.11 (a) UV–Vis spectra of 3: 2 P3HT:$PC_{61}BM$ as-cast PV devices with 0% (solid line), 0.33% (dashed line), 0.67% (dotted line), 1.6% (dashed–dotted line), 3.2% (short dashed line), and 6.3% (solid line) nitrobenzene added into the CB solvent. Offset from the other spectra is the as-cast PV device from the *o*-xylene dispersion (triangles). (b) *j–V* curves of as-cast (upper) and heat-treated (lower) 3: 2 P3HT:$PC_{61}BM$ devices. The devices were cast from CB-amorph (triangles), *o*-xylene-amorph (circles), *o*-xylene-np (squares), and CB/NtB (stars). (From Ref. [81].)

The volume fraction of P3HT aggregates in a P3HT:$PC_{61}BM$ solution could be increased from 60 up to 100% with increasing NtB content (Figure 1.11). Photovoltaic devices from P3HT:$PC_{61}BM$ mixtures with NtB addition resulted in device efficiencies of 4% without further thermal annealing. These experiments proved that a good part of the thin-film morphology can already be introduced on the solution level.

A further example was presented by Park *et al*. using blends of acetophenone and mesitylene [53]. The boiling point difference of MS (165 °C) and AP (202 °C) resulted in an increase of concentration of AP during solvent evaporation. The external quantum efficiency nearly doubled from a maximum of 35% at 500 nm for pure MS to 69% for the solvent blend as can be seen in Figure 1.12. One of the difficulties was obtaining the same drying conditions as *o*-DCB, which limited the ability to fully match the film thickness for different solvent blends. The better device performance of the solvent blended systems was assumed to result from lower series resistance and a superior morphology improving phase separation of P3HT and $PC_{61}BM$ that was analyzed by AFM measurements. The higher boiling point and lower evaporation rate of AP could facilitate reorganization or increase crystallinity.

Oleic acid (OA) was also reported to improve microstructure and device performance of P3HT:$PC_{61}BM$ devices [82]. After thermal annealing, the P3HT:$PC_{61}BM$ blend film with OA showed bigger domain sizes and roughness compared to films without OA. This is a result of enlarged P3HT domains with higher crystallinity analyzed by AFM and XRD measurements. The addition of OA improves the heteromolecular mixture in the solution and induces molecular local ordering in the resulting film. This allowed the formation of well-organized films with high mobility, resulting in high device performance up to 4.3%.

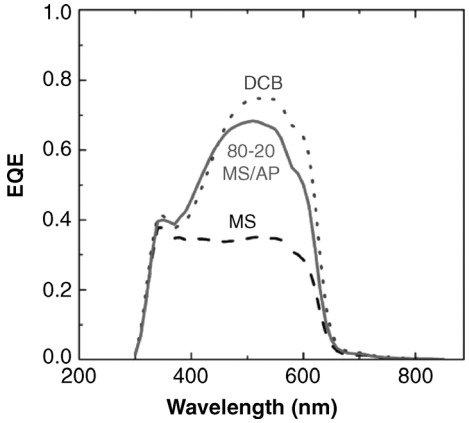

Figure 1.12 EQE measurement data for devices fabricated from *o*-DCB, MS, and 80 vol.% MS–20 vol.% AP mixture. (From Ref. [53].)

1.3.2.5 **Processing Additives**

One approach to control the morphology is the addition of small amounts of a high boiling point solvent with selected solubility into a host solvent. The advantages for this type of processing additives are the easy application to polymers with high and low solubility and the fact that no additional processing step is necessary [83]. For example, additives such as alkylthiols or diiodoalkanes are known to selectively help fullerene aggregation due to a better fullerene solubility compared to polymers [17, 84].

Peet *et al*. analyzed the influence of chain length of different alkane dithiols on the efficiency of P3HT:PC_{61}BM and PCPDTBT:PC_{71}BM solar cells [17]. Small concentrations of alkanethiols formed P3HT aggregations and modified the P3HT:PC_{61}BM phase separation [85]. Since for PCPDTBT thermal or solvent annealing was not successful, additives were used. Addition of 1,8-octanedithiol into CB led to a redshift film absorption peak around 800 nm. This shift to lower energies was associated with enhanced π–π^* stacking and indicated a PCPDTBT phase with more strongly and improved local structural order as compared to films processed from pure CB. Different chain lengths of alkane dithiols were analyzed. Best cell performance was achievable for the longest alkyl chain, 1,8-octanedithiol, resulting in cell efficiencies of up to 5.5%. AFM pictures showed that a specific chain length is necessary for morphological differences. While for butanedithiol no changes were recognizable compared to no additive processing, hexanedithiol addition showed larger domains.

Lee *et al*. investigated the use of processing additives on PCPDTBT:PC_{71}BM organic solar cells [84]. Morphological control could be achieved with the criteria of a selective, differential solubility of the fullerene component and a higher boiling point compared to the host solvent. For the additive, different functional end groups of a 1,8-di(R)octane were used, achieving best results of 5.12 and 4.66% for R = I or Br, respectively. Figures 1.13 and 1.14 show the *j*–*V* curves of the devices with different additives and the schematic depiction of the role of additives, respectively.

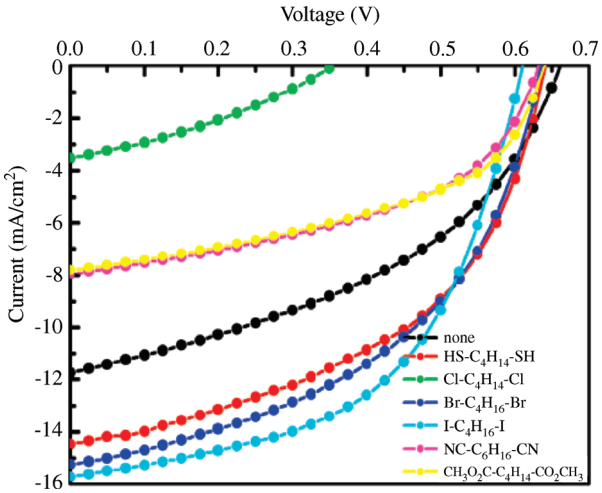

Figure 1.13 *j–V* characteristics of PCPDTBT/$PC_{71}BM$ composite films with various additives: none (black), 1,8-octanedithiol (red), 1,8-dicholorooctane (green), 1,8-dibromooctane (blue), 1,8-diiodooctane (cyan), 1,8-dicyanooctane (magenta), and 1,8-octanediacetate (yellow). (Adapted from Ref. [84].)

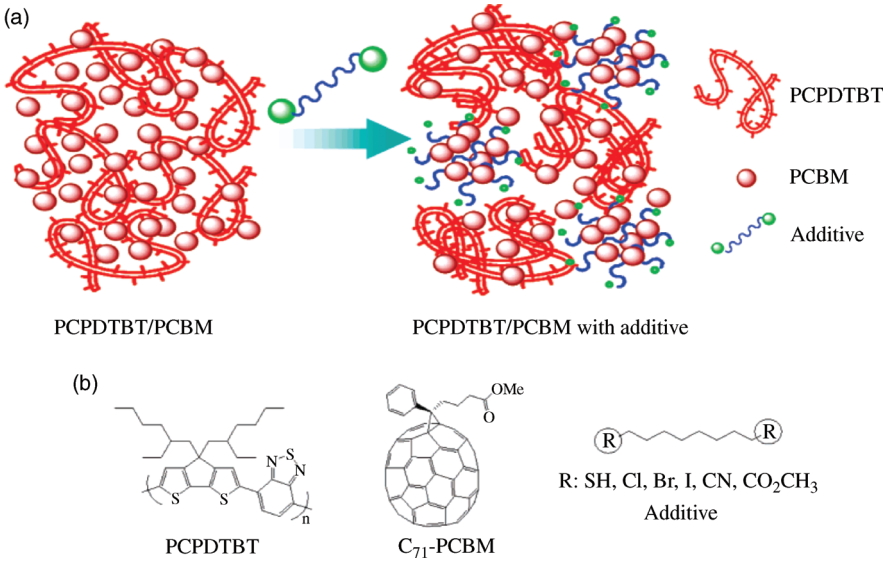

Figure 1.14 Schematic depiction of the role of the processing additive in the self-assembly of bulk heterojunction blend materials (a) and structures of PCPDTBT, $PC_{71}BM$, and additives (b). (Adapted from Ref. [84].)

Moet *et al.* found by modeling the photocurrent that the use of 1,8-octanedithiol can prevent recombination-limited photocurrent in PCPDTBT:$PC_{61}BM$ solar cells [86]. Modeling showed that the decay rate of bound electron–hole pairs is reduced by additive addition resulting in dissociation probability of 70% at short-circuit current.

The use of processing additives was further investigated by Su *et al.* for the polymer poly-{bi(dodecyl)thiophene-thieno[3,4-*c*]pyrrole-4,6-dione} (PBTTPD) in the system PBTTPD:$PC_{71}BM$ [87]. Diiodoalkanes with different chain lengths were added to chloroform solutions and analyzed with GISAXS and GIWAXS measurements. It was concluded that addition of the diiodoalkanes led to an improved dispersion of the $PC_{71}BM$ domains and, therefore, a better network morphology by reducing the grain boundaries of the $PC_{71}BM$-rich phases. Diiodohexane (DIH) provided the finest dispersion of $PC_{71}BM$, due to a balance of solubility for $PC_{71}BM$ and the interactions between additive and the polymer molecules. By using DIH, the polymer crystallinity could be increased and the device performance was improved from 5 to 7.3%.

Further GIWAXS measurements including the use of additives were investigated by Rogers *et al.* who used PCPDTBT in combination with $PC_{71}BM$ and diiodooctane or octanedithiol [83]. By using additives, the device performance could be increased from 3.2 to 5.5%. Both additives have a higher boiling point compared to the host solvent CB and the ability to solvate $PC_{71}BM$. Absorption measurements suggested increased chain aggregation and improved electrical properties were suggested from mobility and photoresponsivity measurements.

The role of additives in polymer crystallinity was further investigated by Agostinelli *et al.* using octanedithiol (ODT) for PCPDTBT:$PC_{71}BM$ films [88]. By using GIXRD, absorption spectroscopy, variable angle spectroscopic ellipsometry (VASE), and time-of-flight (TOF) hole mobility measurements, the degree of order was analyzed and accompanied by transient photovoltage (TPV) measurements changes in device performance were monitored. Upon addition of ODT, the polymer crystallinity was increased, resulting in higher charge pair generation efficiency. A series of polymers with alternating thieno[3,4-*b*]thiophene and benzodithiophene units was investigated by Liang *et al.* [89]. By using *o*-DCB/1,8-diiodooctane (97/3, v/v) as solvent, a more finely distributed polymer/fullerene interpenetrating network was obtained and a significantly enhanced solar cell conversion efficiency of up over 6% was achieved.

Chu *et al.* used a low-bandgap alternating copolymer of 4,4-bis(2-ethylhexyl) dithieno[3,2-*b*:2′,3′-*d*]silole and *N*-octylthieno[3,4-*c*]pyrrole-4,6-dione (PDTSTPD) and $PC_{71}BM$ as active layer with and without addition of 3% 1,8-diiodooctane (DIO) [90]. Without additive, the device performance dropped significantly below 1.0%. AFM studies of the film morphology showed that $PC_{71}BM$ formed too large isolated domains in the blend film prepared without using DIO. As a result, the J_{SC} dropped from 12.2 to 2.6 mA cm^{-2} and the V_{OC} and FF also decreased significantly. Addition of DIO to the solution resulted in much more uniform and finer domain structure, ideal for an effective polymer:$PC_{71}BM$ interpenetrating network. As a result, the device performance was greatly improved up to 6.7%. This finding highlights the importance of morphology control for high-performance solar cells.

Morana *et al.* investigated the effect of ODT on the formation of the charge transfer complex (CTC) for C-PCPDTBT and Si-PCPDTBT [91]. Despite the pristine C-PCPDTBT, no changes were observed in the absorption spectrum of the Si-PCPDTBT films prepared with ODT. Enhanced phase segregation in the C-PCPDTBT films upon addition of ODT caused increase in the molecular luminescence to CT luminescence ratio. This is due to the reduced concentration of CT complexes by a decrease in the contact area between the polymer and the fullerene because of phase separation.

1.3.2.6 **Solution Concentration**

The influence of solution concentration was investigated by Hoppe and Sariciftci with constant mixing ratio of MDMO-PPV and $PC_{61}BM$ [64]. Besides an increase in layer thickness with increasing concentration, also the fullerene cluster size detected by AFM analysis was increased. Further investigations have been performed by Baek *et al.* varying the solution concentration from 1 to 3 wt%. All solid film properties such as the crystalline structure formation, the interchain interaction, and the morphology were influenced [92]. P3HT:$PC_{61}BM$ absorption spectra for as-cast and annealed (150 °C for 10 min) films showed decreasing absorption with increasing concentration. Slower evaporation of the solvent at lower concentration of P3HT:$PC_{61}BM$ leads to better crystallization, stronger interchain interaction, and more ordered phase separation of P3HT. This holds for as-cast as well as for thermally annealed films.

1.3.3 **Conclusive Outlook**

Several approaches have been discussed how the solid-state microstructure of bulk heterojunction composites can be controlled by the design of intelligent solvent systems. Besides the choice of the right solvent, (i) addition of additional good solvents with differing drying properties has been demonstrated to control the domain size of either component, (ii) addition of nonsolvents was shown to trigger the nucleation and subsequent aggregation of individual components, and (iii) addition of processing additives was used to cause a coarsening of the microstructure.

The general ink design for organic semiconductor multicomponent composites is based on a few rules. Generally, the processing solvent has to supply a sufficient solubility, which is typically guaranteed by using halogenated aromatic solvent systems. The processing solvent mainly influences the active layer microstructure. Different $PC_{61}BM$ crystal structures were obtained by using CB, *o*-DCB, or xylene. Low-solubility solvents, in combination with a gradual variation of the surface energy, allow to control a gradient in the vertical phase separation of the two components. The kinetics of drying does impact the size of the aggregates. Slow drying (i.e., high boiling point solvents such as *o*-DCB) creates microstructures with an increased crystallinity as compared to lower boiling point solvents due to enhanced reorganization. Multicomponent solvent systems offer significantly more freedom:

Table 1.1 Solvent parameters of different key solvents for OPV.

Solvent	Hansen solubility parameters, $\delta_D + \delta_P + \delta_H$ ($MPa^{1/2}$)[a]	Molar volume ($m^3\ mol^{-1}$)[a]	Boiling point (°C)[b]	Density ($g\ cm^{-3}$)[b]	Vapor pressure at 25 °C (kPa)[b]
Chlorobenzene	19.0 + 4.3 + 2.0	102.1	131.72	1.1058	1.6
o-Dichlorobenzene	19.2 + 6.3 + 3.3	112.8	180	1.3059	0.18
Chloroform	17.8 + 3.1 + 5.7	80.7	61.17	1.4788	26.2
o-Xylene	17.8 + 1.0 + 3.1	121.2	144.5	0.8802	0.88
Toluene	18.0 + 1.4 + 2.0	106.8	110.63	0.8668	3.79
1,2,4-Trichlorobenzene	20.2 + 6.0 + 3.2	125.5	213.5	1.459	0.057
Cyclohexanone	17.8 + 6.3 + 5.1	104	155.43	0.9478	0.53
Nitrobenzene	20.0 + 8.6 + 4.1	102.7	210.8	1.2037	0.03
1,8-Octanedithiol	17.2 + 6.8 + 6.4[c]	185.6[c]	269[d]	0.97[d]	0.012[d]
1,8-Dibromooctane	17.6 + 4.3 + 2.7[c]	188.6[c]	270[d]	1.477[d]	—

a) Ref. [24].
b) Laboratory solvents and other liquid reagents, in Ref. [93].
c) Ref. [94].
d) Material Safety Data Sheet Sigma–Aldrich.

solvent blends can be used to mimic solubility parameters of a good solvent by using nonhazardous solvents. Furthermore, solvent blends containing high and low vapor pressure solvents allow additional control over the degree of phase separation and interfacial area. Finally, high boiling point additives with selected solubility for one component over the other can trigger more finely distributed microstructures, preventing the aggregation of fullerene clusters. Table 1.1 summarizes the essential parameters for the most frequently used single solvents that are used for processing of organic electronic systems.

1.4 Miscibility

1.4.1 Methods

Miscibility is one essential concept in polymer science, since blended systems are commonly used to address multiple property optimizations as typical for many applications. Several methods can be used to determine the miscibility of two- and more component systems. Morphological investigations of blend systems can easily been done with microscopic methods. Several electron microscopic techniques are used, that is, scanning electron microscopy (SEM), TEM, AFM, and scanning tunneling microscopy (STM). Inhomogeneities are typically

identified by scattering methods. Depending on the required resolution, visual light, X-ray, or neutron scattering methods are used. Neutron scattering is used for investigations in the nanometer domain, X-ray for structures below 1 nm and up to 40 nm, and visual light is used for structures between 100 nm and several microns. The advantage of neutron scattering is the possibility of analyzing also light elements. In the following, we will describe various miscibility aspects for polymer–polymer or polymer–fullerene-based bulk heterojunction composites.

1.4.1.1 Glass Transition

One criterion to distinguish the miscibility of blends is the glass transition temperature (T_g) that can be measured with different calorimetric methods [95]. T_g is the characteristic transition of the amorphous phase in polymers. Below T_g, polymer chains are fixed by intermolecular interactions, no diffusion is possible, and the polymer is rigid. At temperatures higher than T_g, kinetic forces are stronger than molecular interactions and polymer chain diffusion is likely. In binary or multicomponent miscible one-phase systems, macromolecules are statistically distributed on a molecular level. Therefore, only one glass transition occurs, which normally lies between the glass transition temperatures of the pure components. In partly miscible systems, interactions cause a glass transition shift of the pure components toward each other. For immiscible blends, the components are completely separated in different phases and the glass transitions of the pure components remain at their original temperature. Here it is important to emphasize that the appearance of one glass transition is not a measure of complete miscibility rather than a correlation with domain sizes of less than 15 nm. Various examples were discussed elsewhere [95].

1.4.1.2 Surface Energy

The difference in surface energy between two components can be used to define miscibility, as this was identified as one of the driving forces for vertical phase separation. Honda *et al.* analyzed the surface energy to understand the miscibility of P3HT and silicon phthalocyanine derivative (SiPc) – a light-harvesting dye [96]. The surface energy was assessed by contact angle measurements with ultrapure water on spin-coated films. Other studies have suggested as well that the surface energy between P3HT and $PC_{61}BM$ is the driving force for vertical phase separation in the binary blend [97–99]. The surface energies γwere estimated to be 20 and 29 mJ m^{-2} for P3HT and $PC_{61}BM$, respectively, also reported by Jaczewska *et al.* for P3HT [100]. Contrary results were reported by Oh *et al.* and Björström *et al.* with surface energies of 25.79 mJ m^{-2} for P3HT and 39.86 and 38.2 mJ m^{-2} for $PC_{61}BM$ [101, 102]. Nevertheless, SiPc with $\gamma_{SiPc} = 23$ mJ m^{-2} is close to P3HT but has an intermediate value between P3HT and $PC_{61}BM$. Binary blends of P3HT:SiPc and $PC_{61}BM$:SiPc showed that the SiPc molecules do not phase segregate from P3HT, as the surface energy did not change up to 40 wt% SiPc addition (Figure 1.15). On the other hand, SiPc does segregate at the air/film interface from $PC_{61}BM$ as suggested by a

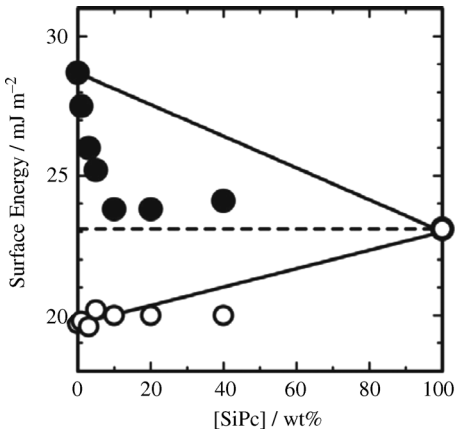

Figure 1.15 Surface energy of P3HT:SiPc (open circles) and $PC_{61}BM$:SiPc (closed circles) blend films plotted against a SiPc content. The broken line represents the surface energy of SiPc (23 mJ m^{-2}). The solid lines represent the surface energy of P3HT:SiPc or $PC_{61}BM$:SiPc predicted on the assumption of homogeneous dispersion of SiPc molecules in blend films. (Adapted from Ref. [96].)

steep decrease of the surface energy at only 10 wt% SiPc addition. Since the component with the lowest surface energy is segregated to the air/film interface, the total energy of the system becomes dominated by a surface layer of the low-energy component. For ternary blends containing P3HT:$PC_{61}BM$:SiPc, the wetting coefficient was used to predict the location of dyes in blend films. This concept was already utilized for the investigation of conductive carbon black particles, carbon nanotubes, $CaCO_3$ nanoparticles, and polymers [103–108]. In case of the ternary organic semiconductor composites, it was found that the SiPc molecules are most likely located at the P3HT:$PC_{61}BM$ interface. SiPc molecules were found to be present in the disordered P3HT phases at the interface between P3HT:$PC_{61}BM$ rather than in the $PC_{61}BM$ and crystal P3HT domains. Thus, the addition of SiPc molecules did not impact the formation of the pristine P3HT and $PC_{61}BM$ phases in the ternary blend films. This is in good agreement with the prediction based on the wetting coefficient, suggesting that the surface energy has a critical impact on such interfacial segregation.

1.4.1.3 **Photoluminescence Quenching**

For the determination of miscibility, the quenching effect of photoluminescence depending on the amount of quencher can be used. Quenching or intermolecular deactivation is the acceleration of the decay rate of an excited state of a material by the presence of another chemical species. The quenching effect is a reduction of PL intensity due to charge transfer to a quencher. The quantum efficiency as a function of quencher concentration can be plotted. A linear quenching represents a statistical distributed content of quencher. If the quenching centers interfere with each other, a saturation regime can be seen.

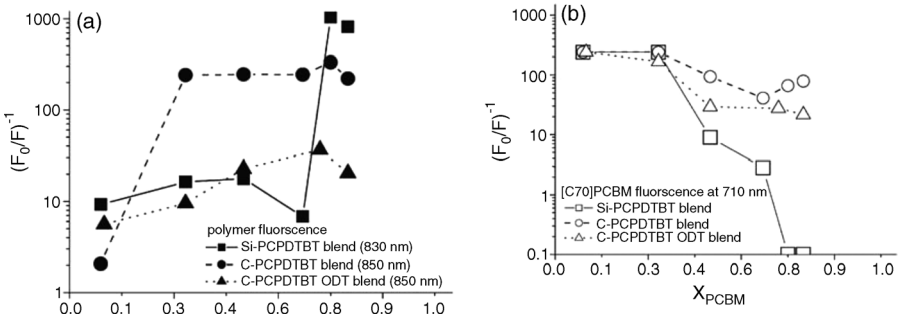

Figure 1.16 Semilogarithmic Stern–Volmer plot ($F_0/F - 1$) of (a) polymer and (b) fullerene fluorescence quenching versus the fullerene content $x_{PC_{71}BM}$ (defined as the weight ratio between the fullerene and the total solid content) for the three polymer:fullerene blends considered: Si-bridged (squares), C-bridged (circles), C-bridged/ODT (triangles). The intensity peaks we considered are positioned at 830 nm for the Si-PCPDTBT and at 850 nm for the C-PCPDTBT polymer, while the $PC_{71}BM$ emission occurs at 710 nm. Since the fullerene fluorescence at 830–850 nm is pronounced, the characteristic fullerene emission spectrum was subtracted from the total measured emission in order to isolate the polymer contribution. The measured fluorescence intensity was then normalized by the corresponding absorbance at the excitation wavelength. The maximum quenching ratio was arbitrarily set as the maximum measured signal (pristine polymer) to noise ratio. (Adapted from Ref. [91].)

According to the Stern–Volmer equation (Eq. (1.8)), the quantum efficiency can be plotted as a function of the quencher concentration, with F_0 as fluorescence intensity without quencher, F as fluorescence intensity with quencher and with the concentration [Q], and K_{SV} as Stern–Volmer constant.

$$\frac{F_0}{F} - 1 = K_{SV}[Q]. \tag{1.8}$$

The mixing behavior of the fullerene in the polymer was studied by measuring the PL of C-bridged PCPDTBT:$PC_{71}BM$ and Si-bridged PCPDTBT:$PC_{71}BM$ blends by Morana *et al.* as shown in Figure 1.16 [91, 109]. The polymer emission is strongly quenched upon addition of $PC_{71}BM$. Using 33 wt% $PC_{71}BM$ in the blend, the spectrally resolved PL signal intensity is decreased by a factor of 200–400 with respect to the one measured for the pure polymer. The quenching yield of $PC_{71}BM$ in PCPDTBT seems to be low compared to other conjugated polymer:fullerene systems [110, 111]. For small $PC_{71}BM$ mass fractions below 0.3 wt%, the total fluorescence intensity of all blends with Si-PCPDTBT and C-PCPDTBT with and without ODT was increasingly quenched with growing fullerene content. Since no emission from the fullerene was observed, it was concluded that the fullerene domain size is smaller than the exciton diffusion length, whereas the polymer domain size is in the range of the exciton diffusion length. The PL quenching studies suggest an increasing trend of phase segregation with growing domain sizes for both the fullerene and the polymers in the order C-PCPDTBT < C-PCPDTBT with ODT < Si-PCPDTBT. The larger extent of phase separation in Si-PCPDTBT was correlated to a

lower solubility of the silicon-bridged polymer in the processing solvent and a stronger tendency to crystallize or aggregate compared to C-PCPDTBT.

Nismy *et al*. analyzed the photoluminescence quenching of carbon nanotubes in P3HT:$PC_{61}BM$ blends and speculated that acid-substituted MWNTs may react as exciton dissociation centers [112]. Excitons created within the exciton diffusion length of a donor:acceptor interface are considered to contribute to the free charge population. Therefore, the BHJ structure consisting of phase-separated donor and acceptor interfaces in the nanoscale range is important for the effective dissociation of excitons into free electron–hole pairs. Carbon nanotubes were added and acted as electron diffusion centers to the pre-existing P3HT:$PC_{61}BM$ BHJ system, for further improving the exciton dissociation by providing triple heterojunction interfaces. Therefore, more dissociated excitons and higher photocurrents were expected.

1.4.2
Polymer–Polymer Miscibility

Polymer–polymer composites are an actively researched section in the field of organic semiconductor composites. Many attempts for blending conjugated polymers for OPV applications and creating a composite microstructure with small (i.e., few nm to few tens of nm) domains were run by the Cambridge group. Granström *et al*. used a cyano derivative of poly(*p*-phenylene vinylene) (MEH-CN-PPV) as electron acceptor and a derivative of polythiophene as hole acceptor [113]. By AFM imaging, the formation of islands of the minority phase was detected, which were larger in size for the thermally treated polythiophene-rich film. In the cross section of a laminated structure, interpenetration between the two layers following the lamination and annealing procedure was recognized, with a length scale of 20–30 nm. Finer scale interpenetration was not revealed. Polyfluorene-based polymer blends consisting of poly(2,7-(9,9-di-*n*-octylfluorene-*alt*-benzothiadiazole)) (F8BT) and poly(2,7-(9,9-di-*n*-octylfluorene)-*alt*-(1,4-phenylene-((4-*sec*-butylphenyl)imino)-1,4-phenylene)) (TFB) were investigated by Kim *et al*. [114]. AFM images are shown in Figure 1.17. A microscale lateral phase separation was recognizable, but the phase-separated domains were not pure at the submicron length scale. Furthermore, a nanoscale vertical phase separation was found. McNeill *et al*. investigated blends of the polymers P3HT and poly((9,9-dioctylfluorene)-2,7-diyl-*alt*-[4,7-bis(3-hexylthiophen-5-yl)-2,1,3-benzothiadiazole]-20,200-diyl) (F8TBT) [115]. Annealing was found to be responsible for coarsening of the phase separation and increase in hole mobility of the P3HT phase, both contributing to an improved charge separation.

Different approaches to mix insulating thermoplasts with organic semiconductors have been made with the aim to combine semiconducting properties of conjugated polymers with excellent mechanical properties of commodity polymers. Goffri *et al*. blended P3HT with polystyrene showing a crystallinity-induced favorable phase separation. Blending P3HT and PS results in vertically stratified structures with dominantly semiconductor at the surface. Application as active layer in

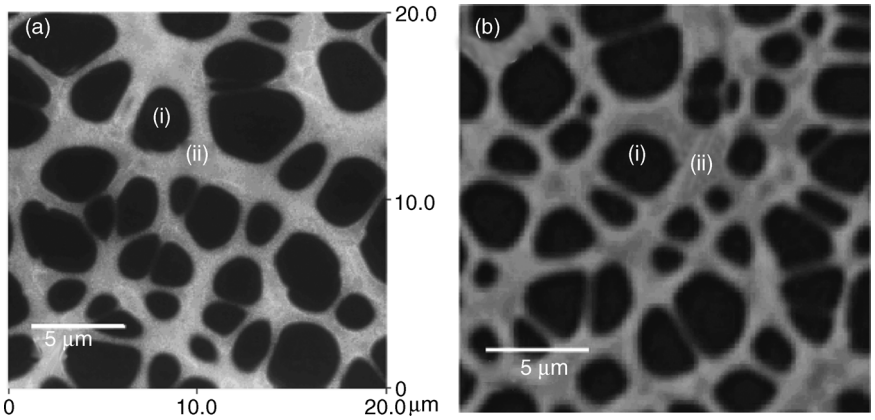

Figure 1.17 (a) AFM image with a 100 nm height scale (white: high region; black: low region) and (b) PL image of 100 nm thick F8BT: TFB (50 : 50) film (domain (i), TFB-rich region; domain (ii), F8BT-rich region). On the basis of the PL of the blend film, it is concluded that the high ridges are F8BT matrix phase (bright regions, domain (ii)) and the thin regions are TFB-rich enclosed phase (dark regions with very weak F8BT emission, domain (i)). (Reprinted with permission from Ref. [114]. Copyright 2004, American Chemical Society.)

organic field-effect transistors showed no degradation of device performance, which is a decisive advantage compared to the use of blends of P3HT with amorphous insulating polymers. Crystalline–crystalline/semiconducting–insulating multicomponent systems offer the possibility to realize high-performance semiconducting systems with reduced material cost, better mechanical properties, and improved environmental stability [116, 117].

Brabec *et al.* [118] blended MDMO-PPV with various nonconjugated binders such as PS, PMMA, and PC and found that addition of up to 10% of an inert polymer does not negatively influence the device performance. Ternary blends containing P3HT:$PC_{61}BM$ blended with insulating polymers such as high-density polyethylene (HDPE) were also investigated by Ferenczi *et al.* [119]. By blending of the donor–acceptor components into the conventional polymer matrix, the percolation threshold for photovoltaic response of the three-component systems is found to be determined by percolation of the fullerene in the polymer matrix [120–122]. Up to 50 wt% of insulating semicrystalline polymers were added to a P3HT: $PC_{61}BM$ blend without decreasing the device performance. The advantages of such ternary systems over the binaries without inert polymeric additives are facilitated processing, enhanced mechanical properties, and increased thickness of the active layer, which reduce defects in the films and improve large-area processing.

Spinodal decomposition has been found for spin-coated films of the ferroelectric random copolymer poly(vinylidene fluoride–trifluoroethylene) (P(VDF-TrFE)) and regioirregular (rir) P3HT. The blend separates into amorphous rir-P3HT domains embedded in a crystalline P(VDF-TrFE) matrix [123]. The number of domains decreases with increasing rir-P3HT content, indicating coarsening of morphology.

1.4.3
Polymer–Fullerene Miscibility

Intercalation of fullerene molecules in a conjugated polymer matrix was reported by Koppe *et al.* and was later on investigated in great detail by the Stanford group [124]. Intercalation of fullerenes in a polymer matrix results in a microstructure where individual fullerene molecules get dissolved in or close to the polymer backbone. Intercalation is dominantly facilitated by voids between the side chains along the polymer backbone and depends on the polymer structure instead of the polymer configuration. The principle of intercalation is shown in Figures 1.18 and 1.19. Intercalation has significant impact on the performance of bulk heterojunction devices, since a significant fraction of fullerenes being dissolved in the polymer is lost for electron transport. The general findings are that polymer with a tendency toward intercalation requires a significantly higher fullerene concentration to guarantee well-balanced transport. Mayer *et al.* have observed fullerene

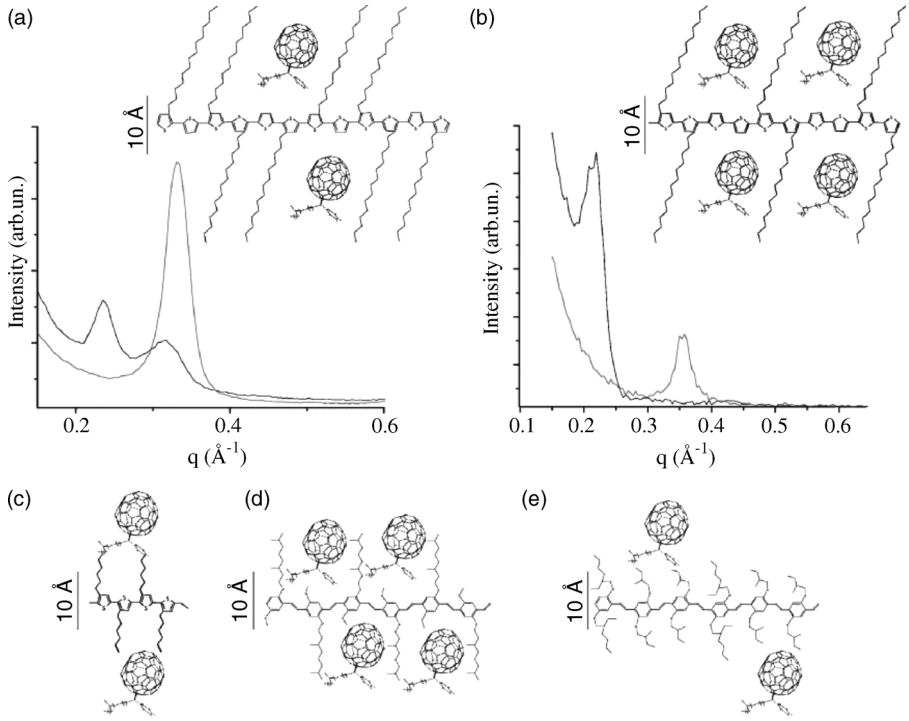

Figure 1.18 Fullerene intercalation in other polymer:fullerene systems. (a) The X-ray diffraction pattern demonstrates an expansion of the *d*-spacing of the pTT (gray line) upon the addition of $PC_{61}BM$ (black line) and the inset shows how the $PC_{61}BM$ fits between the side chains. (b) The same situation exists for PQT as demonstrated by the X-ray pattern. (c) There is insufficient room between the side chains of P3HT to allow for intercalation. (d) There is sufficient room for $PC_{61}BM$ intercalation between the side chains in amorphous MDMO-PPV. (e) $BisOC_{10}$-PPV, however, does not have sufficient room. (From Ref. [125].)

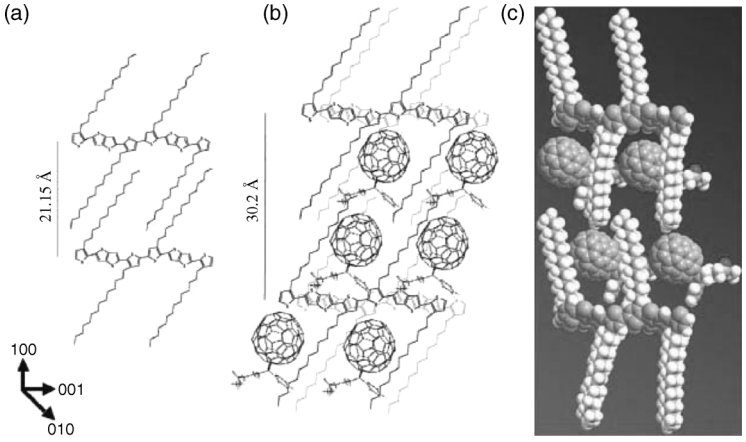

Figure 1.19 Schematic of possible structures showing the effect of $PC_{71}BM$ intercalation on the crystal lattice of pBTTT. (a) The tilt angle for the pristine pBTTT crystal and the amount of interdigitation of the side chains are set to make the *d*-spacing agree with X-ray diffraction. (b) The $PC_{71}BM$ is placed within the intercalated pBTTT:$PC_{71}BM$ in order to agree with the *d*-spacings found in X-ray scattering. (c) The total volume taken up by the electron orbitals using a space-filling routine from ChemBio3D Ultra shows that there is still sufficient room for the intercalation demonstrated in (b). The tilt of the side chains in (c) is only approximate because the simulations do not account for intermolecular interactions. The lattice axes are shown in the lower left corner for reference. (From Ref. [125].)

intercalation in blends with various amorphous and semicrystalline polymers when there is enough free volume between the side chains to accommodate the fullerene molecule [125].

Intercalation of fullerenes between side chains mostly determines the optimum polymer:fullerene blending ratios. These findings offer explanations why large-scale phase separation occurs in some polymer:fullerene blend ratios while thermodynamically stable mixing on the molecular scale occurs for others. High fullerene content is necessary to create the phase separation needed for efficient BHJ solar cells, which leads to optimum blend ratios near 1 : 3 to 1 : 4 polymer:fullerene if intercalation occurs. If no intercalation occurs, an optimum near 1 : 1 is usually found.

While no intercalation occurs in the crystalline phase of P3HT, amorphous portions of P3HT and MDMO-PPV contain significant concentrations of $PC_{61}BM$ [126]. Furthermore, depth profiles of P3HT:$PC_{61}BM$ bilayers showed interdiffusion of both materials already after short annealing times. Therefore, pure amorphous phases do not exist in BHJ or annealed bilayer devices. Energy-filtered transmission electron microscopy (EFTEM) and GISAXS measurements were used for morphological investigations, showing local P3HT concentrations in $PC_{61}BM$-rich domains [127]. This was interpreted as partial miscibility. P3HT:$PC_{61}BM$ χ parameter and Flory–Huggins phase diagram, which predicts miscibility for P3HT volume fractions above 0.42, were determined. Flory–Huggins interaction parameter enables quantifying the chemical interactions

between P3HT and $PC_{61}BM$. Miscibility estimates were obtained from measurements of the melting point depression, which were analyzed with differential scanning calorimetric (DSC) experiments. Quantifying the chemical interactions between P3HT and $PC_{61}BM$ through the Flory–Huggins interaction parameter enables the determination of miscibility range for these two components as long as they are amorphous. Miscibility between P3HT and $PC_{61}BM$ suppresses fullerene crystallization. The crystallization of the polymer leads to the characteristic length scales of the mesostructure, whereby crystallization of the polymer can also lead to macroscopic phase separation by enriching the amorphous polymer phase with fullerene beyond the miscibility limit.

1.4.4 Phase Diagrams

The device performance of organic semiconducting composite devices strongly depends on the blend composition. Different approaches to analyze the phase behavior were used to correlate and improve the electric properties. Phase diagrams mainly consist of liquidus and solidus lines separating different phases. For polymers usually liquidus and solidus lines are determined using end melting temperature and peak melting temperature since all crystallites are molten and the crystalline order is broken [128, 129]. The intersection of both lines represents the eutectic point of the phase diagram, with a phase equilibrium where the degree of freedom is only selectable in a small range.

Binary organic photovoltaic blends containing poly-(3-alkylthiophene)s (P3ATs) with different side chain lengths and different fullerene derivatives were investigated by Müller *et al.*, Zhao *et al.*, and Kim and Frisbie [130–132]. Binary phase diagrams were reconstructed from DSC measurements, and the device performance of corresponding organic solar cells was analyzed in this phase diagram (Figure 1.20). It was suggested that all systems contain a simple eutecticum. Increasing side chain length of P3AT with poly(3-butylthiophene) (P3BT), P3HT, and poly(3-dodecylthiophene) (P3DDT) leads to a shift of the eutectic temperature T_e to higher P3AT content, accompanied with a decrease of T_e from 220 °C for P3BT to 150 °C for P3DDT. For P3HT, a T_e of 205 °C and a eutectic composition c_e of 65 wt% P3HT were found. The maximum J_{SC} of the corresponding devices was found around the eutectic composition, being slightly shifted to higher $PC_{61}BM$ ratios. The higher melting temperature of $PC_{71}BM$ compared to $PC_{61}BM$ results in a higher eutectic temperature of the binary blend with P3HT, which is also slightly shifted to higher P3HT contents compared to $PC_{61}BM$. This is also reflected in the J_{SC} maximum.

Ballantyne and coworkers investigated the blend system poly(3-hexylselenothiophene) (P3HS) with $PC_{61}BM$ by DSC and found a simple eutectic behavior with a eutectic composition c_e of 66 wt% P3HS and a T_e of 230 °C. A high crystallinity of P3HS was found by DSC, but P3HS:$PC_{61}BM$ blend films showed a lower degree of crystallinity than P3HT:$PC_{61}BM$ according to XRD measurements. Therefore, larger fractions of $PC_{61}BM$ can be dissolved in the polymer. The lower degree of

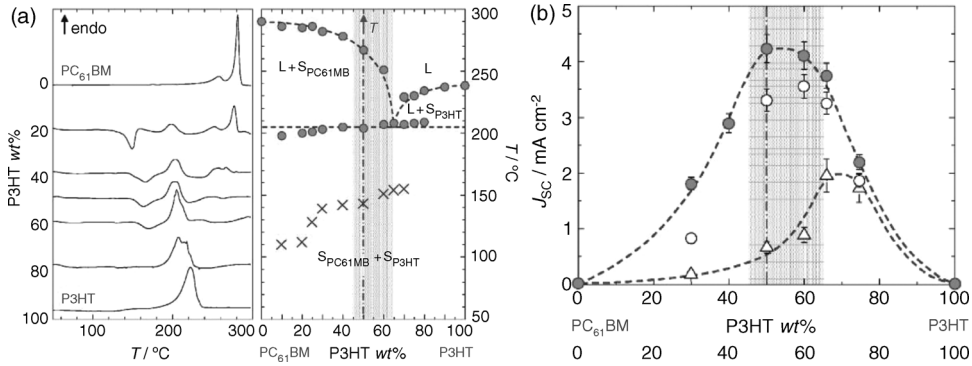

Figure 1.20 (a) Phase behavior of P3HT:$PC_{61}BM$. (a) DSC heating thermograms (left) and corresponding (nonequilibrium) temperature/composition diagram of the P3HT:$PC_{61}BM$ system (right) featuring simple eutectic phase behavior (peak eutectic temperature, $T_e \sim 205\,^{\circ}C$; eutectic composition, $c_e \sim 65$ wt% P3HT). Liquidus lines were constructed with end melting and end dissolution temperatures of neat components and excess component, respectively. Crosses represent the onset of recrystallization; highlighted areas in this and following part indicate the range of composition of optimum device performance. (b) Dependence of short-circuit current density J_{SC} (top panel) and power conversion efficiency (bottom panel) (under simulated solar illumination AM 1.5, 71 mW cm^{-2}) on P3HT/$PC_{61}BM$ blend composition for devices thermally treated at 140 °C after spin casting (filled circles), subsequently melt quenched from 290 °C (open triangles), and then after further annealing at 140 °C (open circles). In accordance with previous reports, J_{SC} is optimized after annealing at blend compositions comprising 50–60 wt% of the polymer. Error bars represent estimated percentage error based on comparison of similar devices. (From Ref. [130].)

phase segregation is likely to contribute to the faster recombination kinetics in the P3HS:$PC_{61}BM$ compared to P3HT:$PC_{61}BM$ blend devices.

Müller *et al.* investigated the phase behavior of liquid-crystalline polymer:fullerene blends [133]. For poly[2,7-(9,9-dioctylfluorene)-*alt*-5,5-(40,70-di-2-thienyl-20,10,30-benzothiadiazole)] (F8TBT, also abbreviated as APFO-3 or PFDTBT) blended with $PC_{61}BM$, a eutectic phase behavior with a eutectic composition c_e of 75 wt% F8TBT at a eutectic temperature T_e of 138 °C was found. The glass transition temperature T_g was found to be independent of composition, showing good match with T_g of the pure components. Above the glass transition temperature, $PC_{61}BM$ crystals tend to nucleate. Miscibility of fullerene in the polymer strongly depends on the molecular weight of the macromolecule. Molecular weight is found to have a significant influence on morphology of P3HT. For P3HT:$PC_{61}BM$ blends, high molecular weight enhances intermolecular ordering (π-stacking) of P3HT. Increased molecular weight leads to extended crystallites and therefore better charge carrier mobility. A threshold for the molecular weight of P3HT was found to be necessary to guarantee sufficient device performance. This threshold was found by investigating various molecular weight fractions of a P3HT master batch [134]. On the other hand, with increasing weight average molecular weight (M_w), the crystallinity of P3HT and the crystalline orientation decreased [135]. This

phenomenon was attributed to transition from a fully extended all-*trans* conformation to a semicrystalline system with crystalline lamellae and amorphous extended interlamellar zones. Huang *et al.* investigated the influence of molecular weight of poly[(4,4′-bis(2-ethylhexyl)dithieno[3,2-*b*:2′,3′-*d*]silole)-2,6-diyl-*alt*-(5,5′-thienyl-4,4′-dihexyl-2,2′-bithiazole)-2,6-diyl] (Si-PCPDTTBT) and $PC_{61}BM$ on morphology [136]. AFM and TEM images showed the increasing phase separation with increasing molecular weight leading to an interpenetrating network for carrier transport and device improvement.

Ternary systems were investigated to further enhance the spectral response of organic solar cells [137, 138]. Small amounts of PCPDTBT were added to the P3HT:$PC_{61}BM$ blend to expand the absorption spectra toward the near-infrared region. Different requirements for such ternary systems have to be fulfilled. The absorption in the near-infrared region should be complementary to the absorption spectra of P3HT. Further, the electronic levels of the sensitizer need to be aligned with respect to those of P3HT and $PC_{61}BM$ to facilitate an efficient photoinduced charge transfer between all components. Finally, the miscibility of such systems is of interest for morphological studies. Ternary phase diagrams for P3HT, PCPTDTBT, and $PC_{61}BM$ were investigated by Li *et al.* as shown in Figure 1.21 using DSC [138]. The phase diagram of the binary system P3HT:$PC_{61}BM$ showed a simple eutectic point, as already reported by Müller *et al.* and Zhao *et al.* [130, 131]. The phase diagram of the ternary system revealed that already small amounts of the dominantly amorphous polymer PCPDTBT can decrease the overall crystallinity but do not affect the position of the eutectic point in ternary blends. A comparison with cell performance showed a correlation of the phase behavior of the binary as well as the ternary blends with its electrical properties in the cells.

1.5 Conclusions

Organic semiconductor composites are a smart concept to design and customize the optoelectronic functionality of a semiconductor by simply blending multiple components with the desired individual properties. This concept is more elegant and technically easily accessible than the design of a single semiconductor compound comprehending all properties. The challenge for organic semiconductor composites is the formulation of suitable inks, the miscibility, and compatibility of the individual inks as well as the control of the solid-state microstructure.

All of these challenges need to be addressed by the formulation of semiconductor composite inks, which is also one of the key parameters for the processing of the active layer of organic photovoltaic devices. Precise information on an ink's rheological properties, the solubility of the individual components, and their influence on solid-state morphology is of highest interest for the development of coating and printing processes. The right choice of the processing solvent, offering good solubility, mainly contributes to the solid-state microstructure of the active layer. Long

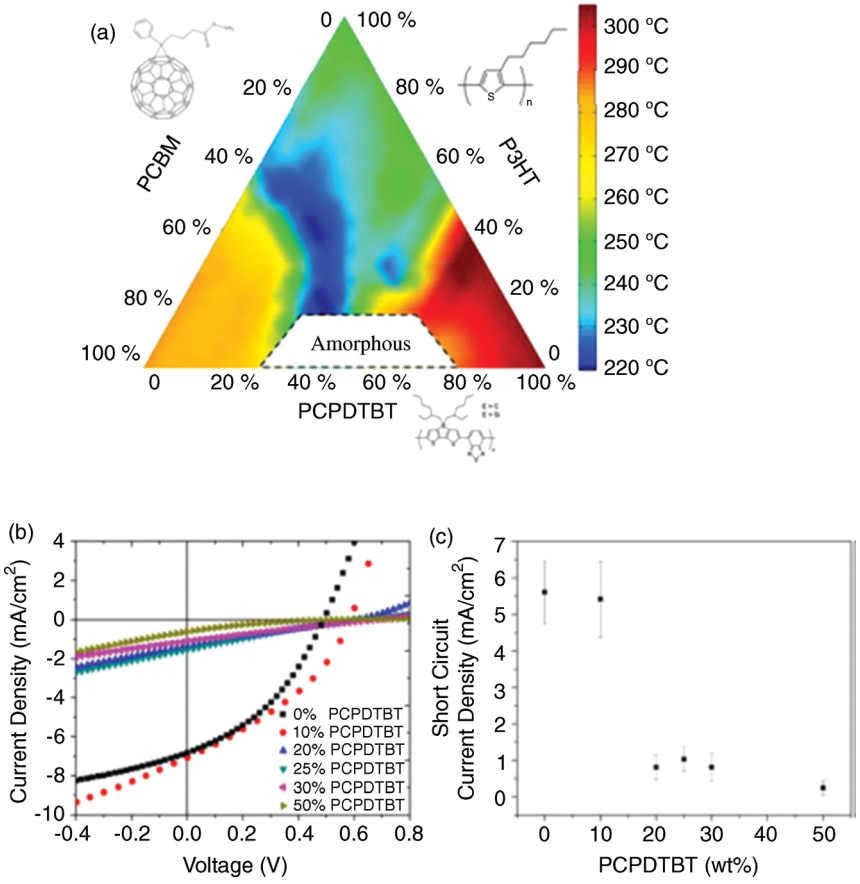

Figure 1.21 (a) Ternary phase diagram with the end melting temperature of the DSC first heating curves as liquidus lines. (b) J_{SC}–V curves of P3HT/PCPDTBT/$PC_{61}BM$ ternary solar cells with a polymer:fullerene ratio of 50 : 50 (w/w). (c) J_{SC} of photovoltaic devices depends on PCPDTBT ratio for ternary blends with a constant fullerene ratio of 50 wt% (total polymer:fullerene 1 : 1). The solar cells were tested under AM 1.5, 100 mW cm^{-2} illumination. (Adapted from Ref. [138].)

drying times typically enhance the polymer crystallinity offering better possibilities for self-assembling of the polymer chains. Different approaches to control the composite's microstructure were investigated by using solvent blends. Among these concepts, the use of additional solvents with high boiling points has led to finer phase separations and therefore increasing device efficiencies. Further research activities have focused on the formation of aggregates by the addition of nonsolvents, favoring crystallinity increase in the solid state. Another task is the use of halogen-free, nonhazardous solvents for industrial processing. Here the formulation of solvent blends using Hansen solubility parameters is becoming established as a reference method.

Miscibility of the components is required to design functional semiconductor composites. Specifically, bulk heterojunction solar cells require precise control of the blend microstructure to guarantee good device efficiency. Polymer–polymer miscibility is ways more complex and difficult than polymer–fullerene miscibility. In the case of polymer–fullerene blends, the intercalation of fullerene within the side chains of conjugated polymers is found as one of the parameters defining the optimum polymer–fullerene ratio. Blending semiconducting and insulating polymers has also been proven to ease industrial production. Establishing phase diagrams and correlation with material and device properties has helped to improve the miscibility of multicomponent composites.

References

1 Brabec, C.J. (2004) *Sol. Energy Mater. Sol. Cells*, **83**, 273–292.
2 Thompson, B.C. and Fréchet, J.-M.J. (2008) *Angew. Chem.*, **120**, 62–82.
3 Chiang, C.K., Fincher, C.R., Park, Y.W., Heeger, A.J., Shirakawa, H., Louis, E.J., Gau, S.C., and MacDiarmid, A.B. (1977) *Phys. Rev. Lett.*, **39**, 1098–1101.
4 Kalinowski, J. (2004) *Organic Light-Emitting Diodes: Principles, Characteristics, and Processes*, Optical Engineering, vol. **91**, CRC Press, New York.
5 Dimitrakopoulos, C.D. and Malenfant, P. R.L. (2002) *Adv. Mater.*, **14** (2), 99–117.
6 Kroon, R., Lenes, M., Hummelen, J.C., Blom, P.W.M., and de Boer, B. (2008) *Polym. Rev.*, **48**, 531–582.
7 Dennler, G., Scharber, M.C., and Brabec, C.J. (2009) *Adv. Mater.*, **21**, 1323–1338.
8 Deibel, C. and Dyakonov, V. (2010) *Rep. Prog. Phys.*, **73**, 096401.
9 Hertel, D. and Baessler, H. (2008) *Chem. Phys. Chem.*, **9**, 666–688.
10 Chamberlain, G.A. (1983) *Sol. Cells*, **8**, 47–83.
11 Tang, C.W. (1986) *Appl. Phys. Lett.*, **48**, 183–185.
12 Yu, G., Gao, J., Hummelen, J.C., Wudl, F., and Heeger, A.J. (1995) *Science*, **270**, 1789–1791.
13 Frohne, H., Shaheen, S.E., Brabec, C.J., Müller, D.C., Sariciftci, N.S., and Meerholz, K. (2002) *Chem. Phys. Chem.*, **9**, 795–799.
14 Hoppe, H. and Sariciftci, N.S. (2004) *J. Mater. Res.*, **19**, 1924–1945.
15 McGehee, M.D. and Topinka, M.A. (2006) *Nat. Mater.*, **5**, 675–676.
16 Seong, J.Y., Chung, K.S., Kwak, S.K., Kim, Y.H., Moon, D.G., Han, J.I., and Kim, W.K. (2004) *J. Korean Phys. Soc.*, **45**, 5914.
17 Peet, J., Kim, J.Y., Coates, N.E., Ma, W.L., Moses, D., Heeger, A.J., and Bazan, G.C. (2007) *Nat. Mater.*, **6**, 497–500.
18 Green, M.A., Emery, K., Hisikawa, Y., and Warta, W. (2009) *Prog. Photovolt. Res. Appl.*, **17**, 85–94.
19 Gaudiana, R. and Brabec, C.J. (2008) *Nat. Photon.*, **2**, 287–289.
20 Park, S.H., Roy, A., Beaupré, S., Cho, S., Coates, N., Moon, J.S., Moses, D., Leclerc, M., Lee, K., and Heeger, A.J. (2009) *Nat. Photon.*, **3**, 297–303.
21 Scharber, M.C., Mühlbacher, D., Koppe, M., Denk, P., Waldauf, C., Heeger, A.J., and Brabec, C.J. (2006) *Adv. Mater.*, **18**, 789–794.
22 Brabec, C.J. and Durrant, J. (2008) *MRS Bull.*, **33**, 670.
23 Hildebrand, J.H. and Scott, R.L. (1952) *J. Chem. Phys.*, **20** (10), 1520–1521.
24 Hansen, C.M. (2007) Chapter 1, in *Hansen Solubility Parameters – A User's Handbook*, 2nd edn, CRC Press, Boca Raton, FL.
25 Blanks, R.F. and Prausnitz, J.M. (1964) *Ind. Eng. Chem. Fundam.*, **3**, 1–8.
26 Weimer, R.F. and Prausnitz, J.M. (1965) *Petrol. Refiner*, **44**, 237–242.
27 Hansen, C.M. (1967) *J. Paint Technol.*, **39**, 104–117.

28 Hansen, C.M. (1967) *J. Paint Technol.*, **39**, 505–510.

29 Hansen, C.M. and Skaarup, K. (1967) *J. Paint Technol.*, **39**, 511–514.

30 Small, P.A. (1953) *J. Appl. Chem.*, **3**, 71.

31 Hoy, K.L. (1970) *J. Paint Technol.*, **42**, 76–78.

32 van Krevelen, D.W. (1972) *Properties of Polymers: Correlations with Chemical Structure*, Elsevier, Amsterdam.

33 Coleman, M.M., Serman, C.J., Bhagwagar, D.E., and Painter, P.C. (1990) *Polymer*, **31**, 1187–1203.

34 Fredenslund, A., Gmehling, J., and Rasmussen, P. (1977) *Vapor–Liquid Equilibria Using UNIFAC*, Elsevier, Amsterdam.

35 Gmehling, J. (1998) *Fluid Phase Equilib.*, **144**, 37–47.

36 Derr, E.L. and Deal, C.H. (1969) *Inst. Chem. Eng. Symp. Ser.*, **3**, 40.

37 Klamt, A. and Schüürmann, G. (1993) *J. Chem. Soc., Perkin Trans. 2*, **5**, 799–805.

38 Jork, C., Kristen, C., Pierccini, D., Stark, A., Chiappe, C., Beste, Y.A., and Arlt, W. (2005) *J. Chem. Thermodyn.*, **37** (6), 537–558.

39 Klamt, A. (1995) *J. Phys. Chem.*, **99** (7), 2224–2235.

40 Klamt, A. (1998) COSMO and COSMO-RS, in *Encyclopedia of Computational Chemistry* (ed. P.v.R. Schleyer), John Wiley & Sons, Ltd, Chichester.

41 Klamt, A., Jonas, V., Bürger, T., and Lohrenz, J.C.W. (1998) *J. Chem. Phys. A*, **102** (26), 5074–5085.

42 Klamt, A. (2005) *COSMO-RS: From Quantum Chemistry to Fluid Phase Thermodynamics and Drug Design*, Elsevier, Amsterdam.

43 Paul, D.R. and Barlow, J.W. (1981) *Polym. Eng. Sci.*, **21**, 985–996.

44 Robeson, L.M. (2007) Chapter 2: Fundamentals of polymer blends, in *Polymer Blends*, Hanser, Munich.

45 Flory, P.J. (1962) *Principles of Polymer Chemistry*, Cornell University Press, Ithaca, NY.

46 Walker, B., Tamayo, A., Duong, D.T., Dang, X.-D., Kim, C., Granstrom, J., and Nguyen, T.-Q. (2011) *Adv. Energy Mater.*, **1** (2), 221–229.

47 Machui, F., Abbott, S., Waller, D., Koppe, M., and Brabec, C.J. (2011) *Macromol. Chem. Phys.*, **212**, 2159–2165.

48 Ruoff, R.S., Tse, D.S., Malhotra, R., and Lorents, D.C. (1993) *J. Phys. Chem.*, **97**, 3379–3383.

49 Yu, G., Gao, J., Hummelen, J.C., Wudl, F., and Heeger, A.J. (1995) *Science*, **270**, 1789–1791.

50 Kronholm, D. and Hummelen, J. (2007) *Mater. Matters*, **2**, 16–20.

51 Troshin, P., Hoppe, H., Renz, J., Egginger, M., Mayorova, J., Goryachev, A., Peregudov, A., Lyubovskaya, R., Gobsch, G., Sariciftci, N.S., and Razumov, V. (2009) *Adv. Funct. Mater.*, **19**, 779–788.

52 Hansen, C.M. and Smith, A.L. (2004) *Carbon*, **42**, 1591–1597.

53 Park, C.-D., Fleetham, T.A., Li, J., and Vogt, B.D. (2011) *Org. Electron.*, **12**, 1465–1470.

54 Lee, K.-G., Kim, J.Y., Park, S.H., Kim, S. H., Cho, S., and Heeger, A.J. (2007) *Adv. Mater.*, **19**, 2445–2449.

55 Ma, W.-L., Yang, C.-Y., Gong, X., Lee, K.-H., and Heeger, A.J. (2005) *Adv. Funct. Mater.*, **15**, 1617–1622.

56 Zhao, Y., Yuan, G., Roche, P., and Leclerc, M. (1995) *Polymer*, **36**, 2211–2214.

57 Mihailetchi, V.D., Xie, H.-X., de Boer, B., Popescu, L.M., Hummelen, J.C., and Blom, P.W.M. (2006) *Appl. Phys. Lett.*, **89**, 012107.

58 Chu, C.-W., Yang, H.-C., Hou, W.-J., Huang, J.-S., Li, G., and Yang, Y. (2008) *Appl. Phys. Lett.*, **92**, 103306.

59 Miller, E.W. and Miller, R.M. (1989) *Environmental Hazards: Air Pollution. A Reference Handbook*, ABC-Clio, Santa Barbara, CA.

60 David Cooper, C. and Alley, F.C. (1994) *Air Pollution Control: A Design Approach*, 2nd edn, Waveland Press, Inc., Long Grove, IL.

61 Dang, M.T., Hirsch, L., and Wantz, G. (2011) *Adv. Mater.*, **23**, 3597–3602.

62 Shaheen, S.E., Brabec, C.J., Sariciftci, N. S., Padinger, F., Fromherz, T., and Hummelen, J.C. (2001) *Appl. Phys. Lett.*, **78**, 841–843.

63 Hoppe, H., Niggemann, M., Winder, C., Kraut, J., Hiesgen, R., Hinsch, A., Meissner, D., and Sariciftci, N.S. (2004) *Adv. Funct. Mater.*, **14**, 1005–1011.

64 Hoppe, H. and Sariciftci, N.S. (2006) *J. Mater. Chem.*, **16**, 45–61.

65 Rispens, M.T., Meetsma, A., Rittberger, R., Brabec, C.J., Sariciftci, N.S., and Hummelen, J.C. (2003) *Chem. Commun.*, 2116–2118.

66 Ruderer, M., Guo, S., Meier, R., Chiang, H., Körstgens, V., Wiedersich, J., Perlich, J., Roth, S., and Müller-Buschbaum, P. (2011) *Adv. Funct. Mater.*, **21**, 3382–3391.

67 Yu, H. (2010) *Synth. Met.*, **160**, 2505–2509.

68 Kwong, C., Djurišić, A., Chui, P., Cheng, K., and Chan, W. (2004) *Chem. Phys. Lett.*, **384**, 372–375.

69 Park, S.H., Roy, A., Beaupré, S., Cho, S., Coates, N., Moon, J.S., Moses, D., Leclerc, M., Lee, K.-H., and Heeger, A.J. (2009) *Nat. Photon.*, **3**, 297–303.

70 Jaczewska, J., Budkowski, A., Bernasik, A., Moons, E., and Rysz, J. (2008) *Macromolecules*, **41**, 4802–4810.

71 Berson, S., De Bettignies, R., Bailly, S., and Guillerez, S. (2007) *Adv. Funct. Mater.*, **17**, 1377–1384.

72 Hoth, C.N., Choulis, S.A., Schilinsky, P., and Brabec, C.J. (2007) *Adv. Mater.*, **19**, 3973–3978.

73 Hoth, C.N., Schilinsky, P., Choulis, S.A., and Brabec, C.J. (2008) *Nano Lett.*, **8**, 2806–2813.

74 Kawano, K., Sakai, J., Yahiro, M., and Adachi, C. (2009) *Sol. Energy Mater. Sol. Cells*, **93**, 514–518.

75 Lange, A., Wegener, M., Boeffel, C., Fischer, B., Wedel, A., and Neher, D. (2010) *Sol. Energy Mater. Sol. Cells*, **94**, 1816–1821.

76 Chen, F.-C., Tseng, H.-C., and Ko, C.-J. (2008) *Appl. Phys. Lett.*, **92**, 103316.

77 Zhang, F.-L., Jespersen, K.G., Björström, C., Svensson, M., Andersson, M.R., Sundström, V., Magnusson, K., Moons, E., Yartsev, A., and Inganäs, O. (2006) *Adv. Funct. Mater.*, **16**, 667–674.

78 Wang, Z., Wang, E., Hou, L., Zhang, F., Andersson, M., and Inganäs, O. (2011) *J. Photon. Energy*, **1**, 011122.

79 Alem, S., Chu, T., Tse, S., Wakim, S., Lu, J., Movileanu, R., Tau, Y., Belanger, F., Desilets, D., Beaupre, S., Leclerc, M., Rodman, S., Waller, D., and Gaudiana, R. (2011) *Org. Electron.*, **12**, 1788–1793.

80 Park, Y.D., Lee, H.S., Chio, Y.J., Kwak, D., Cho, J.H., Lee, S., and Cho, K. (2009) *Adv. Funct. Mater.*, **19**, 1200–1206.

81 Moulé, A.J. and Meerholz, K. (2008) *Adv. Mater.*, **20**, 240–245.

82 Wang, W., Wu, H., Yang, C., Luo, C., Zhang, Y., Chen, J., and Cao, Y. (2007) *Appl. Phys. Lett.*, **90**, 183512.

83 Rogers, J., Schmidt, K., Toney, M., Kramer, E., and Bazan, G. (2011) *Adv. Mater.*, **23**, 2284–2288.

84 Lee, J.K., Ma, W.L., Brabec, C.J., Yuen, J., Moon, J.S., Kim, J.Y., Lee, K., Bazan, B. C., and Heeger, A.J. (2008) *J. Am. Chem. Soc.*, **130**, 3619–3623.

85 Peet, J., Soci, C., Coffin, R.C., Nguyen, T. Q., Mikhailovsky, A., Moses, D., and Bazan, G.C. (2006) *Appl. Phys. Lett.*, **89**, 252105.

86 Moet, D., Lenes, M., Morana, M., Azimi, H., Brabec, C., and Blom, P. (2010) *Appl. Phys. Lett.*, **96**, 213506.

87 Su, M.-S., Kuo, C.Y., Yuan, M.-C., Jeng, U.-S., Su, C.-J., and Wei, K.-H. (2011) *Adv. Mater.*, **23**, 3315–3319.

88 Agostinelli, T., Ferenczi, T.A.M., Pires, E., Foster, S., Maurano, A., Müller, C., Ballantyne, A., Hampton, M., Lilliu, S., Campoy-Quiles, M., Azimi, H., Morana, M., Bradley, D.D.C., Durrant, J., Macdonald, J.E., Stingelin, N., and Nelson, J. (2011) *J. Polym. Sci. B*, **49**, 717–724.

89 Liang, Y., Feng, D., Wu, Y., Tsai, S.-T., Li, G., Ray, C., and Yu, L. (2009) *J. Am. Chem. Soc.*, **131**, 7792–7799.

90 Chu, T.-Y., Tsang, S.-W., Zhou, J., Verly, P.G., Lu, J., Beaupré, S., Leclerc, M., and Tao, Y. (2011) *Sol. Energy Mater. Sol. Cells*. doi: 10.1016/j.solmat.2011.09.042.

91 Morana, M., Azimi, H., Dennler, G., Egelhaaf, H.-J., Scharber, M., Forberich, K., Hauch, J., Gaudiana, R., Waller, D., Zhu, Z., Hingerl, K., van Bavel, S.S., Loos, J., and Brabec, C.J. (2010) *Adv. Funct. Mater.*, **20**, 1180–1188.

92 Baek, W.-H., Yang, H., Yoon, T.-S., Kang, C.J., Lee, H.H., and Kim, Y.-S. (2009) *Sol. Energy Mater. Sol. Cells*, **93**, 1263–1267.

93 Lide, D.R. (ed.) (2011–2012) *CRC Handbook of Chemistry and Physics*, 92nd edn (Internet version), CRC Press/Taylor & Francis, Boca Raton, FL.

94 Abbott, S., Hansen, C.M., and Yamamoto, H. (2008–2011) Hansen Solubility Parameters in Practice, (software) version 3.1.17, www.hansen-solubility.com (accessed October 2011).

95 Robeson, L.M. (2007) Chapter 5; Characterization of polymer blends, in *Polymer Blends*, Hanser, Munich.

96 Honda, S., Ohkita, H., Benten, H., and Ito, S. (2011) *Adv. Energy Mater.*, **1**, 588–598.

97 Campoy-Quiles, M., Ferenczi, T., Agostinelli, T., Etchegoin, P.G., Kim, Y., Anthopoulos, T.D., Stavrinou, P.N., Bradley, D.D.C., and Nelson, J. (2008) *Nat. Mater.*, **7**, 158–164.

98 Orim, A., Masuda, K., Honda, S., Benten, H., Ito, S., Ohkita, H., and Tsuji, H. (2010) *Appl. Phys. Lett.*, **96**, 043305.

99 Germack, D.S., Chan, C.K., Kline, R.J., Fischer, D.A., Gundlach, D.J., Toney, M. F., Richter, L.J., and DeLongchamp, D.M. (2010) *Macromolecules*, **43**, 3828–3836.

100 Jaczewska, J., Raptis, I., Budkowski, A., Goustouridis, D., Raczkowska, J., Sanopoulou, M., Pamula, E., Bernasik, A., and Rysz, J. (2007) *Synth. Met.*, **157**, 726–732.

101 Oh, J.Y., Jang, W.S., Lee, T.I., Myoung, J.-M., and Baik, H.K. (2011) *Appl. Phys. Lett.*, **98**, 023303.

102 Björström, C.M., Bernasik, A., Rysz, J., Budkowski, A., Nilsson, S., Svensson, M., Andersson, M.R., Magnosson, K.O., and Moons, E. (2005) *J. Phys.: Condens. Matter*, **17**, L529–L534.

103 Sumita, M., Sakakta, K., Asai, S., Miyasaka, K., and Nakagawa, H. (1991) *Polym. Bull.*, **25**, 265–271.

104 Wu, M. and Shaw, L. (2006) *J. Appl. Polym. Sci.*, **99**, 477–488.

105 Göldel, A., Kasaliwal, G., and Pätschke, P. (2009) *Macromol. Rapid Commun.*, **30**, 423–429.

106 Caudouin, A.-C., Devaux, J., and Bailly, C. (2010) *Polymer*, **51**, 1341–1354.

107 Ma, C.G., Zhang, M.Q., and Rong, M.Z. (2007) *J. Appl. Sci.*, **103**, 1578–1584.

108 Cheng, T.W., Keskkula, J., and Paul, D.R. (1992) *Polymer*, **33**, 1606–1619.

109 Morana, M., Wegscheider, M., Bonanni, A., Kopidakis, N., Shaheen, S., Scharber, M., Zhu, Z., Waller, D., Gaudiana, R., and Brabec, C. (2008) *Adv. Funct. Mater.*, **18**, 1757–1766.

110 Haugeneder, A., Neges, M., Kallinger, C., Spirkl, W., Lemmer, U., Feldmann, J., Scherf, U., Harth, E., Gügel, A., and Müllen, K. (1999) *Phys. Rev. B*, **59**, 15346–15351.

111 van Duren, J., Yang, X., Loos, J., Bulle-Lieuwma, C., Sieval, A., Hummelen, J.C., and Janssen, R.A.J. (2004) *Adv. Funct. Mater.*, **14**, 425–434.

112 Nismy, N.A., Jayawardena, K.D.G., Adikaari, A.A.D., and Silva, S.R.P. (2011) *Adv. Mater.*, **23**, 3796–3800.

113 Granström, M., Petritsch, K., Arias, A.C., Lux, A., Andersson, M.R., and Friend, R. H. (1998) *Nature*, **395**, 297–260.

114 Kim, J.S., Ho, P.K.H., Murphy, C.E., and Friend, R.H. (2004) *Macromolecules*, **37**, 2861–2871.

115 McNeill, C.R., Halls, J.J.M., Wilson, R., Whiting, G.L., Berkebile, S., Ramsey, M. G., Friend, R.H., and Greenham, N.C. (2008) *Adv. Funct. Mater.*, **18**, 2309–2321.

116 Goffri, S., Müller, C., Stingelin-Stutzmann, N., Breiby, D.W., Radano, C. P., Andreasen, J.W., Thompson, R., Janssen, R.A.J., Nielsen, M.M., Smith, P., and Sirringhaus, H. (2006) *Nat. Mater.*, **5**, 950–956.

117 Babel, A. and Jenekhe, S.A. (2004) *Macromolecules*, **37**, 9835–9840.

118 Brabec, C.J., Padinger, F., Sariciftci, N.S., and Hummelen, J.C. (1999) *J. Appl. Phys.*, **85**, 6866–6872.

119 Ferenczi, T., Müller, C., Bradley, D., Smith, P., Nelson, J., and Stingelin, N. (2011) *Adv. Mater.*, **23**, 4093–4097.

120 Müller, C., Goffri, S., Breiby, D.W., Andreasen, J.W., Chanzy, H.D., Janssen, R.A.J., Nielsen, M.M., Radano, C.P., Sirringhaus, H., Smith, P., and Stingelin-

Stutzmann, N. (2007) *Adv. Funct. Mater.*, **17**, 2674–2679.
121 Wolfer, P., Müller, C., Smith, P., Baklar, M.A., and Stingelin-Stutzmann, N. (2007) *Synth. Met.*, **157**, 827–833.
122 Kumar, A., Baklar, M.A., Scott, K., Kreouzis, T., and Stingelin-Stutzmann, N. (2009) *Adv. Mater.*, **21**, 4447–4451.
123 Asadi, K., Wondergem, H.J., Moghaddam, R.S., McNeill, C.R., Stingelin, N., Noheda, B., Blom, P.W.M., and de Leeuw, D.M. (2011) *Adv. Funct. Mater.*, **21**, 1887–1894.
124 Koppe, M., Scharber, M., Brabec, C., Duffy, W., Heeney, M., and McCulloch, I. (2007) *Adv. Funct. Mater.*, **17**, 1371–1376.
125 Mayer, A.C., Toney, M.F., Scully, S.R., Rivnay, J., Brabec, C.J., Scharber, M., Koppe, M., Heeney, M., McCulloch, I., and McGehee, M.D. (2009) *Adv. Funct. Mater.*, **19**, 1173–1179.
126 Collins, B., Gann, E., Guignard, L., He, X., McNeill, C., and Ade, H. (2010) *J. Phys. Chem. Lett.*, **1**, 3160–3166.
127 Kozub, D., Vakhshouri, K., Orme, L., Wang, C., Hexemer, A., and Gomez, E. (2011) *Macromolecules*, **44**, 5722–5726.
128 Ehrenstein, G.W., Riedel, G., and Trawiel, P. (2003) *Praxis der Thermischen Analyse von Kunststoffen 2*, Aufl. Carl Hanser Verlag, München.
129 Wunderlich, B. (1990) *Thermal Analysis*, Academic Press, San Diego, CA.
130 Müller, C., Ferenczi, T., Campoy-Quiles, M., Frost, J., Bradley, D., Smith, P., Stingelin-Stutzmann, N., and Nelson, J. (2008) *Adv. Mater.*, **20**, 3510–3515.
131 Zhao, J., Swinnen, A., Van Assche, G., Manca, J., Vanderzande, D., and Van Mele, B. (2009) *J. Phys. Chem. B*, **113**, 1587–1591.
132 Kim, J.Y. and Frisbie, C.D. (2008) *J. Phys. Chem. C*, **112**, 17726–17736.
133 Müller, C., Bergqvist, J., Vandewal, K., Tvingstedt, K., Anselmo, A., Magnusson, R., Alonso, M., Moons, E., Arwin, H., Campoy-Quilles, M., and Inganäs, O. (2011) *J. Mater. Chem.*, **21**, 10676–10684.
134 Zen, A., Saphiannikova, M., Neher, D., Grenzer, J., Grigorian, S., Pietsch, U., Asawapirom, U., Janietz, S., Scherf, U., Lieberwirth, I., and Wegner, G. (2006) *Macromolecules*, **39**, 2162–2171.
135 Brinkmann, M. and Rannou, P. (2007) *Adv. Funct. Mater.*, **17**, 101–108.
136 Huang, J.H., Chen, F.-C., Chen, C.-L., Huang, A.T., Hsiao, Y.-S., Teng, C.-M., Yen, F.-W., Chen, P., and Chu, C.W. (2011) *Org. Electron.*, **12**, 1755–1762.
137 Koppe, M., Egelhaaf, H.-J., Dennler, G., Scharber, M.C., Brabec, C.J., Schilinsky, P., and Hoth, C.N. (2010) *Adv. Funct. Mater.*, **20**, 338–346.
138 Li, N., Machui, F., Waller, D., Koppe, M., and Brabec, C.J. (2011) *Sol. Energy Mater. Sol. Cells*, **95**, 3465–3471.